Draft version November 11, 2025
Typeset using LaTeX **twocolumn** style in AASTeX7.0.1

A JWST/NIRSpec Integral Field Unit Survey of Luminous Quasars at z ∼ 5–6 (Q-IFU): Rest-frame Optical Nuclear Properties and Extended Nebulae

Weizhe Liu (刘伟哲),[1] Xiaohui Fan,[1] Huan Li,[2] Richard Green,[1] Jaclyn B. Champagne,[1] Xiangyu Jin,[1] Jianwei Lyu,[1] Maria Pudoka,[1] Wei Leong Tee,[1,3] Feige Wang,[4] Jinyi Yang,[4] Yongda Zhu,[1] and Nayera Abdessalam[1]

[1] *Steward Observatory, University of Arizona, 933 N. Cherry Ave., Tucson, AZ 85721, USA*
[2] *School of Aerospace Science and Technology, Xidian Univerisity, Xian, Shaanxi, 710126 China*
[3] *Department of Astronomy and Astrophysics, The Pennsylvania State University, 525 Davey Lab, University Park, PA 16802, USA*
[4] *Department of Astronomy, University of Michigan, 1085 S. University Ave., Ann Arbor, MI 48109, USA*

ABSTRACT

It remains debatable how billion-solar-mass supermassive black holes (SMBHs) form and evolve within the first billion years. We report results from a James Webb Space Telescope (JWST)/NIRSpec integral field unit (IFU) survey of 27 luminous quasars at $z \sim 5$–6, enabling a systematic investigation of their key physical properties and the associated, extended line emission. Our sample hosts SMBHs with $\log(M_{\rm BH}/M_\odot) \sim 8.6$–9.7 and Eddington ratios of ~ 0.1–2.6 based on Hβ, and the Hβ-based and Hα-based BH mass are broadly consistent with each other. Our sample may have a slightly smaller median BH mass and larger median Eddington ratio than lower-redshift quasars within the same luminosity range, although the difference could still be explained by statistical uncertainties. They generally follow the empirical correlations between [O III] λ5007 equivalent width and bolometric luminosities or Eddington ratios formed by lower-redshift quasars. The majority of them fall within the Eigenvector 1 planes formed by lower-redshift quasars. Nevertheless, a subset of the sample shows enhanced, blueshifted [O III] emission associated with fast outflows. Spatially extended [O III] line emission is detected in 6 objects and shows morphologies and kinematics consistent with merging activities and/or turbulent and clumpy interstellar media (ISM). Tentative evidence of quasar radiative feedback shaping the ISM of a merging companion galaxy is seen in the object with the most extended [O III] emission. Our results provide crucial insight into the rapid growth of SMBHs and the gaseous environments they reside in at z ∼ 5–6.

1. INTRODUCTION

Luminous quasars powered by $\sim 10^8$–10^{10} $M_\odot$ supermassive black holes (SMBH) are already in place within ∼1 billion years after the Big Bang. It remains unclear how they grow so rapidly (e.g., Volonteri 2012; Wu et al. 2015; Bañados et al. 2018; Matsuoka et al. 2019; Onoue et al. 2019; Shen et al. 2019; Yang et al. 2021; Schindler et al. 2020; Wang et al. 2021; Farina et al. 2022; Fan et al. 2023). To deepen our understanding of the early growth of such giants, it is crucial to obtain reliable measurements of their BH mass. For high-z Type 1 quasars, BH masses are usually obtained using the single-epoch virial method, which assumes virial motions for the line-emitting gas within the broad line region (BLR). The BLR sizes are derived from quasar continuum luminosity following empirical correlations between the two (i.e., the R–L relation), and the conversion from observables to BH mass is further calibrated with AGN with reverberation mapping (RM) BH mass measurements. Rest-frame UV and optical broad emission lines, C IV λ1549, Mg II λ2800, Hα, and Hβ, are the workhorses for virial BH mass measurements (e.g., McLure & Jarvis 2002; McLure & Dunlop 2004; Vestergaard 2002; Vestergaard & Peterson 2006a; Greene & Ho 2005; Shen et al. 2011; Barth et al. 2015; Dietrich et al. 2002, 2009; Dietrich & Hamann 2004; Netzer et al. 2004; Sulentic et al. 2004, 2006; Greene et al. 2010; Assef et al. 2011; Ho et al. 2012; Runnoe et al. 2013; Brotherton et al. 2015; Plotkin et al. 2015; Shemmer & Lieber 2015; Zuo et al. 2015). Among them, Hβ is deemed the most reliable tracer based on comparisons with both RM-based BH mass and other single-epoch virial BH mass estimators (e.g., Shen & Liu 2012; Shen 2013).

Corresponding author: Weizhe Liu
wzliu@arizona.edu

At z$\gtrsim$5, BH masses are mainly derived from Mg II λ2800 or C IV λ1549 in the rest-frame UV (e.g Yang et al. 2021; Schindler et al. 2020) due to the challenge of observing faint objects beyond the K-band. With the advent of JWST, high S/N rest-frame optical spectra can be obtained efficiently (e.g., Marshall et al. 2023; Yang et al. 2023; Loiacono et al. 2024; Decarli et al. 2024; Liu et al. 2024; Lyu et al. 2025), which starts to confirm the large BH masses of those quasars with the more reliable tracer, Hβ. Additionally, rest-frame optical spectroscopy allows for close examinations of empirical correlations, like Eigenvector 1 (EV1; e.g., Boroson & Green 1992) and "Baldwin effect" (e.g., Baldwin 1977), which reflect fundamental properties of BH accretion. Furthermore, it also unveils the size and kinematics of narrow line region (NIR) through emission lines like [O III] λ5007 (e.g., Netzer et al. 2004; Nesvadba et al. 2008; Carniani et al. 2015; Liu et al. 2013; Perna et al. 2015; Shen 2016; Liu et al. 2020, 2024; Vayner et al. 2023; Yang et al. 2023, and references therein). It is therefore imperative to investigate the rest-frame optical spectral properties of z$\gtrsim$5 quasars statistically and compare them with those of the lower-redshift objects.

In Liu et al. (2025), we introduced a JWST cycle 2 NIRSpec/integral field unit (IFU) survey program #3428 (; PI W. Liu), which observed 27 luminous quasars at z $\sim$ 5–6. In that paper, we presented novel results on the detection of more frequent extreme galaxy-scale outflows in the z $\sim$ 5–6 quasars from the survey program than in the lower-z quasars. In this work, we report other key rest-frame optical spectral properties of these z $\sim$ 5–6 quasars and their host galaxies/companion galaxies from the same program. This paper is organized as follows. In Section 2, we describe the sample selection, observations and data reduction. In Section 3, the spectral fitting and analysis are presented. The discussion on the quasar nuclear spectral properties and extended line emission is presented in 4 and 5, respectively. Finally, our main conclusions are summarized in Section 6. Throughout the paper, we assume a ΛCDM cosmology with $H_0 = 70$ km s^{-1} Mpc^{-1}, $\Omega_{\rm m} = 0.3$, and $\Omega_\Lambda = 0.7$. An arcsecond corresponds to 5.71–6.45 kpc at the redshifts of our objects.

2. SAMPLE SELECTION, OBSERVATION AND DATA REDUCTION

The sample selection, observations and data reduction are described in detail in Liu et al. (2025). In the following, we briefly summarize their key aspects.

Our objects are observed with JWST NIRSpec/IFU mode (Böker et al. 2022; Jakobsen et al. 2022) through the JWST cycle 2 survey program #3428 (Q-IFU; PI W. Liu). The parent sample consists of 100 spectroscopically-confirmed luminous quasars at two narrow redshift ranges z $\sim$ 4.74 – 4.88 and z $\sim$ 5.66 – 6 with absolute magnitude at rest-frame 1450 Å $M_{1450} \lesssim -25.5$, which are randomly chosen from the sources published in Pâris et al. (2017); Wang et al. (2016); Fan et al. (2023) to maximize the sky coverage. The redshift windows are chosen to place key spectral features (Hβ, [O III], Fe, etc) in the sweet spots of the NIRSpec gratings. In the end, we obtained data for 27 objects, which are randomly chosen from the parent sample based on JWST scheduling. Their locations on the redshift vs M_{1450} plane are shown in Fig. 1. The sources at z $\sim$ 4.74–4.88 and z $\sim$ 5.66–6 are observed in configurations G235H/F170LP and G395H/F290LP, with corresponding wavelength coverage of 1.66–3.05 and 2.87–5.14 μm, respectively. The gratings have a nominal resolving power $\lambda/\Delta\lambda \simeq 2700$, corresponding to a velocity resolution $\sim$ 110 km s^{-1}. We use a 2-point small cycling dither pattern and a NRSIRS2RAPID readout pattern. The total on-source exposure time is 466.8s per target, which gives a 3-σ limiting surface brightness of $\sim 1\times10^{-17}$ erg s^{-1} cm^{-2} Å^{-1} arcsec^{-2} at rest-frame 5008 Å. The field-of-view (FoV) of the IFU observations is $\sim 3'' \times 3''$. The data are available on the Mikulski Archive for Space Telescopes (MAST) at the Space Telescope Science Institute, which can be accessed via 10.17909/s4b6-ng62.

The IFU data were reduced following the general 3 stages of JWST Science Calibration Pipeline (version "1.14.0" and the context file "jwst_1293.pmap"), combined with customized software and scripts to replace or improve certain steps in the public pipeline. Specifically, after stage 1, we subtract the correlated detector noise ($1/f$ noise) in the count rate images using NSCLean (Rauscher 2024). After stage 2, we apply further sigma-clipping in each calibrated 2D spectral images to remove outliers (Vayner et al. 2023; Veilleux et al. 2023; Liu et al. 2024, 2025). The final IFU data cube is reconstructed with the "drizzle" method adopting a spatial pixel (spaxel) size of 0$''$.1, and a master background is built from the spaxels covering the blank sky and then subtracted. The final quasar spectrum is extracted from each IFU data cube with r=0$''$.1–0$''$.5 apertures to maximize the S/N of their spectra and remove artificial spectral oscillations. Aperture correction is applied to each spectrum based on the curve of growth analysis results from the NIRSpec/IFU data of the standard star TYC 4433-1800-1 (proposal ID: 1128) over the same wavelength range.

3. SPECTRAL ANALYSIS

3.1. *Spectral Fitting*

3.1.1. *Hβ, Hγ, and* [O III] *region*

The details of spectral fitting in this region can be found in Liu et al. (2025). We briefly describe the key procedures below. For each object, we adopt the public software, PyQSOFit (Guo et al. 2018; Shen et al. 2019) with additional customized scripts to model the spectrum. Specifically, the quasar pseudo-continuum is fit with a power-law and the empirical Fe II templates from Boroson & Green (1992); Vestergaard & Wilkes (2001). For emission lines, Hβ and Hγ are fit with up to 3 broad Gaussian components and 1 narrow Gaussian component. The kinematics (i.e., the velocity and velocity dispersion) of each corresponding broad Gaussian component in the two lines are tied together. The [O III] doublet is fit with up to 2 Gaussian components where the kinematics of the narrow Gaussian component is tied to those of the narrow Gaussian components of Hβ and Hγ. The only exception is for J0859+2520, where the narrow [O III] λ5007 component is highly blueshifted with respect to Hβ and the kinematics of the two are untied. The number of Gaussian components adopted in the final best-fit model is determined based on the Bayesian information criterion (BIC), where the model with the lowest BIC statistics is adopted. All spectra with their best-fit models can be found in Fig. 11 of the Appendix A.

3.1.2. *Hα region*

For the 12 targets at z $\sim$ 6, Hα emission lines are also covered by our spectra. We fit the quasar pseudo-continuum with the same approach as described in Sec. 3.1.1 and the Hα with up to 3 broad Gaussian components and 1 narrow Gaussian component. For J1141+7114 and J1327+5732, narrow [N II] $\lambda\lambda$6548,6583 and [S II] $\lambda\lambda$6716,6731 emission lines are also detected and fit with 1 narrow Gaussian component with its kinematics tied to that of the narrow Hα. The ratio of the [N II] doublet is set to the theoretical value, 1:3. For J1327+5732, such fit leads to an unphysical [S II] doublet ratio; we set the line widths of the narrow Hα, [N II], and [S II] as the same as those of the narrow Hβ. The best-fits for all of these 12 objects are shown in Fig. 12.

3.2. *Systemic Redshift*

The determination of the systemic velocities of our objects is described in detail in Liu et al. (2025), which is briefly summarized here: whenever [O III] is detected, the systemic redshift is determined from the peak of the relatively narrower [O III] component, if it exists and is not significantly blueshifted with respect to the Hβ emission line. Otherwise, the systemic redshift is determined from the peak of the overall Hβ emission line profile. The final results are listed in Table 1. In Fig. 2, we compare these systemic redshifts with those reported in the literature (Pâris et al. 2017; Wang et al. 2016; Fan et al. 2023), which are mainly based on rest-frame UV emission lines including C IV, C III] and/or Si IV]. We refer the reader to the corresponding references for more detailed descriptions of their redshift determination. Our mean (median) systemic velocities are $\sim$400 ($\sim$40) km s^{-1} larger than those from the UV-based ones, and the largest offsets between the two reach $\sim\pm$4000 km s^{-1}. Such redshift differences are seen in previous studies of lower redshift quasars (e.g., Hewett & Wild 2010; Matthews et al. 2023, and references therein), where the average blueshift of rest-frame UV emission lines is usually attributed to the presence of strong nuclear quasar winds. A more detailed analysis of the differences in

Table 1. Target Information

Object	RA	DEC	$z_{\rm ref}$	ref.	$z_{\rm sys}$
(1)	(2)	(3)	(4)	(5)	(6)
J0732+3256	07:32:31.28	+32:56:18.33	4.760	a	4.771
J0756+0218	07:56:22.37	+02:18:20.17	5.730	b	5.762
J0759+1800	07:59:07.57	+18:00:54.7	4.778	c	4.796
J0807+1328	08:07:15.11	+13:28:05.1	4.870	c	4.880
J0829+0303	08:29:07.62	+03:03:56.56	5.850	b	5.855
J0831+4046	08:31:22.57	+40:46:23.3	4.820	c	4.900
J0840+5624	08:40:35.09	+56:24:19.90	5.844	b	5.837
J0850+3246	08:50:48.25	+32:46:47.90	5.870	b	5.830
J0859+2520	08:59:31.29	+25:20:19.5	4.780	c	4.779
J0927+2001	09:27:21.82	+20:01:23.70	5.772	b	5.768
J0941+5947	09:41:08.35	+59:47:25.7	4.861	c	4.860
J0953+6910	09:53:55.90	+69:10:52.62	5.840	b	5.918
J1050+4627	10:50:05.11	+46:27:35.5	4.844	c	4.837
J1100+5800	11:00:41.94	+58:00:01.3	4.776	c	4.759
J1102+6635	11:02:47.29	+66:35:19.6	4.803	c	4.787
J1116+5853	11:16:33.75	+58:53:22.04	5.730	b	5.721
J1134+3928	11:34:15.21	+39:28:26.0	4.795	c	4.826
J1141+7119	11:41:43.06	+71:19:25.07	5.860	b	5.851
J1245+4348	12:45:10.13	+43:48:37.9	4.820	c	4.890
J1257+6349	12:57:57.47	+63:49:37.20	5.950	b	6.012
J1327+5732	13:27:41.33	+57:32:38.43	5.740	b	5.751
J1328+4445	13:28:25.16	+44:45:00.2	4.810	c	4.820
J1342+5838	13:42:43.46	+58:38:50.0	4.855	c	4.852
J1436+5007	14:36:11.74	+50:07:06.90	5.850	b	5.840
J1458+3327	14:58:05.99	+33:27:23.0	4.830	c	4.851
J1620+5202	16:20:45.64	+52:02:46.65	4.790	a	4.791
J1621+5155	16:21:00.92	+51:55:48.79	5.710	b	5.614

NOTE—(4): Redshifts of our objects in the literature. (5): references for column (4): a. Wang et al. (2016) b. Fan et al. (2023), c. Pâris et al. (2017). (6): redshifts determined from our data. See 3.2 for details.

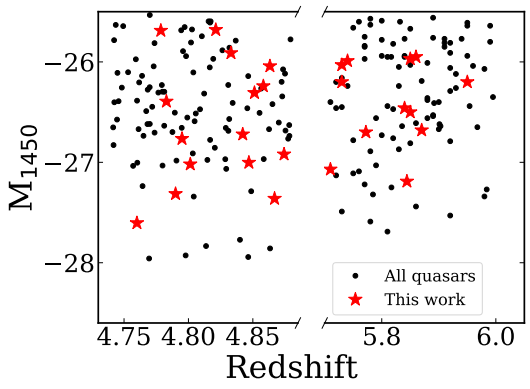

Figure 1. M_{1450} (absolute magnitude at 1450 Å) versus redshift for our objects (red) and all other spectrally-confirmed luminous quasars within the same redshift ranges from the literature (black) in Table 1.

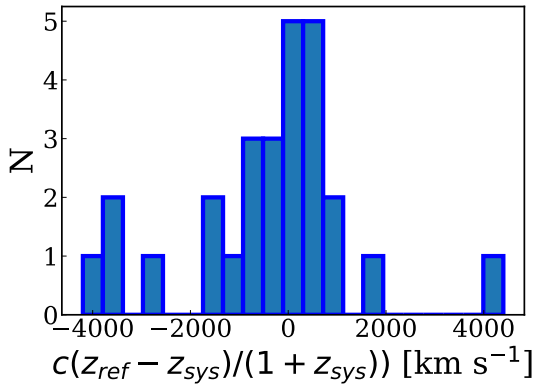

Figure 2. Difference of the systemic redshifts between those determined from our data (z_{sys}) and those from the literature which are based on rest-frame UV emission lines including C IV, C III] and/or Si IV] (z_{ref}).

various redshift determination approaches is deferred to future work.

3.3. *Nuclear Properties*

The bolometric luminosities of our objects are derived adopting 5100Å continuum luminosity ($\lambda L_\lambda(5100)$) with a bolometric correction factor of 9.26 (Richards et al. 2006). The Hβ-based BH masses are derived from the scaling relation in Vestergaard & Peterson (2006b):

$$\log(M_{\rm BH}/M_\odot) = \log\{[\frac{\rm FWHM(H\beta)}{1000\ {\rm km\ s^{-1}}}]^2[\frac{\lambda L_\lambda(5100)}{10^{44}\ {\rm erg\ s^{-1}}}]^{0.5}\} + (6.91 \pm 0.02) \quad (1)$$

Here FWHM(Hβ) are calculated for the entire line profile of the broad Hβ emission line. The Eddington ratios ($\lambda_{\rm Edd}$) are then derived following $L_{\rm Edd} = 1.26\times10^{38}(M_{\rm BH}/M_\odot)\ ergs^{-1}$. Overall, our objects have black hole masses of $\log(M_{\rm BH}/M_\odot)$ ~8.6–9.7 and $\lambda_{\rm Edd}$ ~ 0.1–2.6. These Hβ-based measurements are the fiducial values for the BH mass related quantities presented in this paper and are listed in Table 2.

Similarly, whenever possible, we also derive the Hα-based BH mass following (Greene & Ho 2005):

$$\log(M_{\rm BH,H\alpha}/M_\odot) = \log\{(2.0^{+0.4}_{-0.3})[\frac{\rm FWHM(H\alpha)}{1000\ {\rm km\ s^{-1}}}]^{2.06\pm0.06} [\frac{L(\rm H\alpha)}{10^{42}\ {\rm erg\ s^{-1}}}]^{0.55\pm0.02}\} \quad (2)$$

Here FWHM(Hα) are calculated for the entire line profile of the broad Hα emission line. L(Hα) is the luminosity of the broad Hα emission line. These results are also summarized in Table 2.

3.4. *Composite Spectrum*

To compare the spectral properties of our high-redshift quasars with lower-redshift ones, we construct a comparison sample at cosmic noon from Shen (2016) with the same bolometric luminosity range as our sample ($\log(L_{bol}/L_\odot)$~46.7—47.7), which is described in detail in Liu et al. (2025). In short, this comparison sample, referred to as *Shen quasars* hereafter, represents typical Type 1 quasars at z ~ 1.5–3.5 with rest-frame optical spectra of similar S/N to those of our sample. Matching quasar luminosity is essential, as it not only correlates with accretion power but also influences various emission line properties, including the rest-frame equivalent width (REW; e.g., the "Baldwin effect"; Baldwin 1977) and line shapes (e.g., Richards et al. 2002; Shen et al. 2008; Richards et al. 2011). The median composite spectra of our objects and the comparison sample are constructed following a similar approach adopted by Shen (2016) and Vanden Berk et al. (2001). Specifically, each spectrum is first shifted to the rest-frame and normalized by the mean flux density between 4400–5100 Å. The median spectrum of each sample is then built from the normalized spectra. This approach better preserves the relative strength of the emission lines.

As shown in Fig. 3, the composite spectrum of our objects closely resembles that of *Shen quasars*. Our high-z sample shows spectral characteristics fully consistent with luminous, Type 1 quasars, including blue power-law continuum with little dust obscuration, blended broad Fe emission and strong line emission (Balmer lines, [O III] $\lambda\lambda$4959,5007 doublet, etc). A faint [O II] $\lambda\lambda$3726,3729 emission line is tentatively detected (S/N

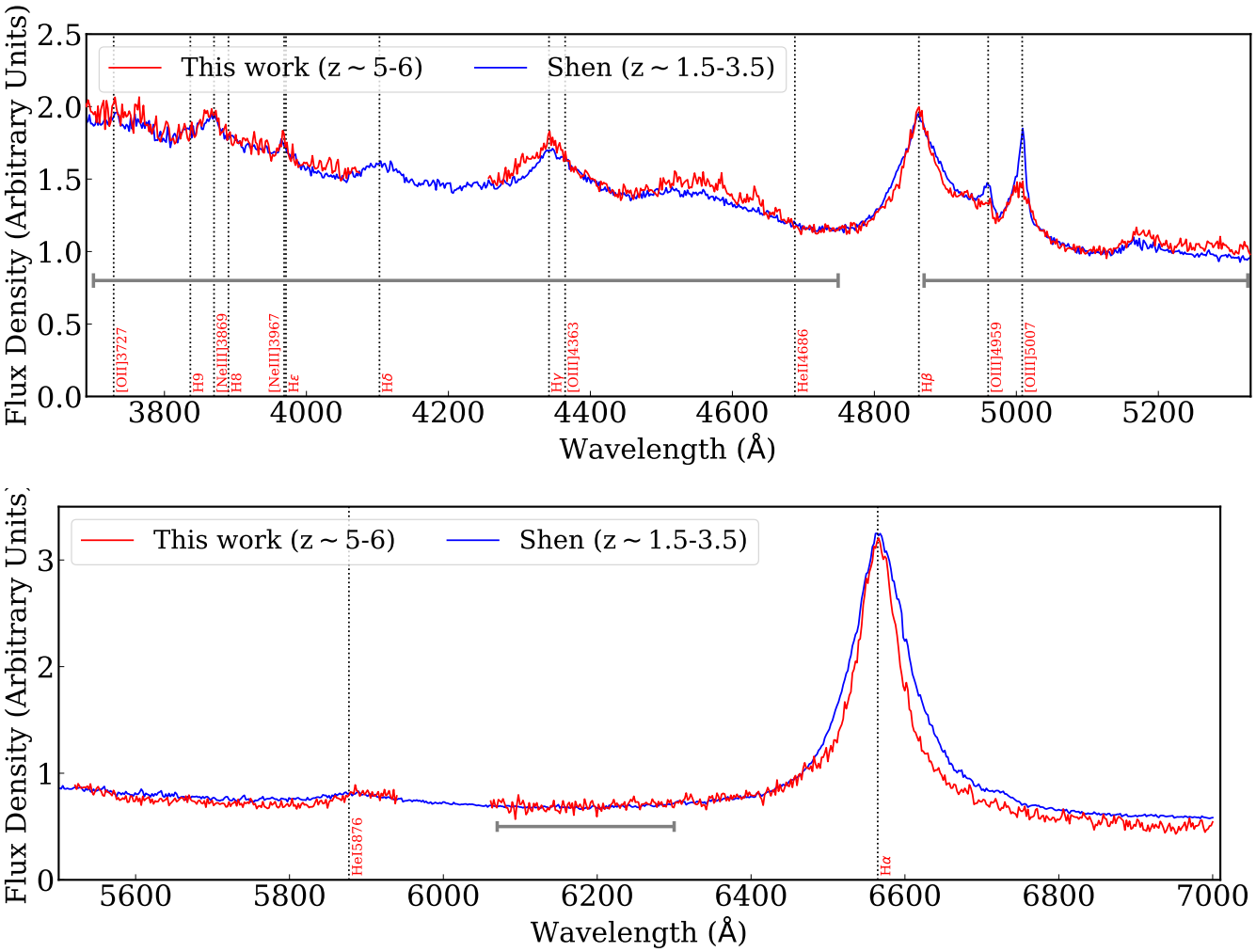

Figure 3. Composite spectra of our z ∼ 5–6 sample (red) and the z ∼ 1.5–3.5 *Shen quasars* matched in the same luminosity range. The two spectra are further normalized at 5100 Å. The locations of the major quasar emission lines are indicated by the dotted lines. The horizontal gray bars indicate the locations of the major blended Fe emission.

∼2) in the composite spectrum, while [N II] and [S II] lines remain undetected. Nevertheless, these faint emission lines are clearly detected in a few objects. For example, [O II] λλ3726,3729 is detected in 1 object, J0807+1328. [N II] and [S II] are detected in 2 objects, J1141+7114 and J1327+5732.

The most prominent difference between the composite spectra of the two samples lies in the [O III] emission lines. They are weaker (with respect to Hβ) but more blueshifted and broader in our sample than those in the *Shen quasars*. As both two samples are matched to the same narrow bolometric luminosity range, the difference in [O III] is not primarily caused by the well-known "Baldwin effect" observed in low-z quasars, a well-known trend of decreasing $EW_{[OIII]}$ with increasing luminosity (e.g., Baldwin 1977; Stern & Laor 2013; Zhang et al. 2013). Instead, the larger blueshift and line width of [O III] in our sample mainly reflect the presence of more frequent fast outflows in our sample as investigated in detail in Liu et al. (2025). We will expand more on this in Sec. 4.3. In addition, more subtle differences between the two composite spectra also exist: For our sample, the Hβ and Hα emission lines are narrower and the Fe emission is stronger.

4. QUASAR SPECTRAL PROPERTIES

4.1. *Hβ Black Hole Mass*

Our data provide reliable, Hβ-based BH masses for our objects for the first time. Overall, our sample exhibits broad Hβ lines with FWHM ∼ 2040 – 7180 km s^{-1} and BH masses with $\log(M_{BH}/M_\odot) \sim 8.6 - 9.7$. The locations of our objects in the bolometric luminosity – BH mass plane are shown in Fig. 4. As expected, our sample occupies the region of high bolometric luminosity (∼ 46.8—47.7) and large BH mass with respect to the overall SDSS z<1 quasar population gathered from

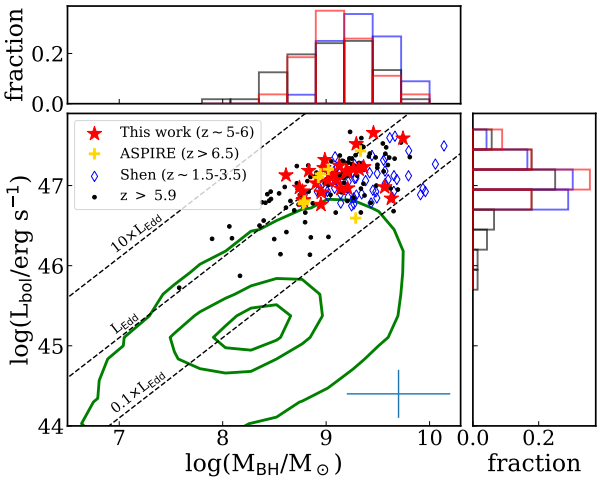

Figure 4. Bolometric luminosity versus BH mass for our objects (red), *Shen quasars* (blue), ASPIRE quasars at z $\sim$ 6.5–6.8 (orange) and all z $>$ 5.9 quasars from Fan et al. (2023, black). The green contours represent the distributions of 99.998%, 90% and 50% of all z $<$ 1 SDSS quasars from Wu et al. (2023). The dashed lines show the locations of constant accretion rates at 0.1, 1 and 10 times the Eddington luminosity. All BH masses are based on Hβ, except for those of quasars from Fan et al. (2023) which are based on Mg II. The typical statistical uncertainties for the bolometric luminosity and Hβ BH mass are indicated by the blue cross. The top and right panels show the fraction histograms for our objects, *Shen quasars* and all z$>$5.9 quasars.

Wu et al. (2023), with high Eddington ratios ($\sim$ 0.1–2.6). They share almost the same BH mass and Eddington ratio ranges as z$>$5.9 quasars with reliable Mg II-based BH mass from Fan et al. (2023) when matched in bolometric luminosity and other high-z quasars with Hβ-based BH mass, like z$>$6.5 ASPIRE quasars (Yang et al. 2023). Our results confirm that these luminous quasars are 10^9 $M_\odot$ SMBHs with high accretion rates within the first $\sim$1 billion years after the Big Bang, which is in line with previous studies at slightly lower (Trakhtenbrot et al. 2011, e.g., z $\sim$ 4.8; Mg II-based BH mass) and higher redshifts (e.g., z$>$6.5; Hβ-based BH mass Yang et al. 2023) drawing the picture that the early emergence of these luminous quasars require continuous/frequent active accretion (see Fan et al. 2023, and references therein).

When compared to the *Shen quasars* at cosmic noon within the same bolometric luminosity range, our objects seem to show, on average, slightly smaller BH mass and higher Eddington ratios: Our sample has median $\log(M_{\rm BH}/M_\odot)$ of 9.1 and median $\lambda_{\rm Edd}$ of 0.9. The *Shen quasars* has median $\log(M_{\rm BH}/M_\odot)$ of 9.3 and median $\lambda_{\rm Edd}$ of 0.4. However, the typical statistical uncertainty of Hβ-based BH mass is on the order of 0.5 dex (e.g. McLure & Jarvis 2002; Vestergaard & Peterson 2006b; Shen 2013). We thus use the Monte Carlo method to estimate the 90% confidence level of the median BH mass and $\lambda_{\rm Edd}$, where we assume that the uncertainties of individual measurements follow a normal distribution with a standard deviation of 0.5 dex. For BH mass $\log(M_{\rm BH}/M_\odot)$, we obtain 8.9–9.3 for our sample and 9.2–9.5 for the *Shen quasars*. For $\lambda_{\rm Edd}$, we obtain 0.5–1.3 for our sample and 0.3–0.5 for the *Shen quasars*. Therefore, the difference between the median BH mass and $\lambda_{\rm Edd}$ of the two samples are insignificant. Overall, our results cannot conclusively prove that the BH mass and $\lambda_{\rm Edd}$ of the two samples are systematically offset from each other.

The rest-frame UV emission line Mg II λ2800 is another widely used single-epoch BH mass estimator of high-z quasars and is accessible from the ground. Only two objects (J0759+1800, J0807+1328) from our sample have reliable Mg II λ2800-based BH mass ($\log(M_{\rm BH}/M_\odot$ = 9.0 and 9.2) from the literature (Trakhtenbrot et al. 2011). They are consistent with the Hβ-based BH masses ($\log(M_{\rm BH}/M_\odot$ = 9.1 and 9.3) derived from our data given the typical statistical uncertainties (0.5 dex) of these BH mass measurements (e.g. McLure & Jarvis 2002; Vestergaard & Peterson 2006b; Shen 2013). This agreement is consistent with the findings from previous studies (e.g., Yang et al. 2023; Marshall et al. 2023; Liu et al. 2024; Loiacono et al. 2024) at similar redshifts where the difference between the two BH mass measurements is up to $\sim$0.5 dex.

4.2. *Hα vs Hβ*

The relative profiles of Hα and Hβ reflect the physical properties of BLR, including their kinematic and ionization structures. In this section, we compare the Hα and Hβ properties for the 12 objects where both lines are covered.

In the left panel of Fig. 5, we compare the FWHMs of the broad Hα and Hβ lines. All 12 objects fall within the rms scatter ($\sim$0.1 dex) of the best-fit relation for a sample of 162 z$\leq$0.35 SDSS quasar with order-of-magnitude lower luminosities ($43\lesssim\log(\lambda L_\lambda(5100))\lesssim46$; Greene & Ho 2005). The average FWHM of broad Hβ ($\sim$4140 km s^{-1}) of our sample is slightly larger than that of broad Hα ($\sim$3530 km s^{-1}). As Hβ is emitted preferentially in regions of higher density and/or higher ionization parameter than Hα (Osterbrock & Ferland 2006) and that line width generally decreases with radius, this suggests that the density or the ionization parameter of the BLR increases with decreasing radii, as is observed in low-z quasars. The mean value of $\rm FWHM_{H\beta}/FWHM_{H\alpha}$ ratio is $\sim$1.17, which is iden-

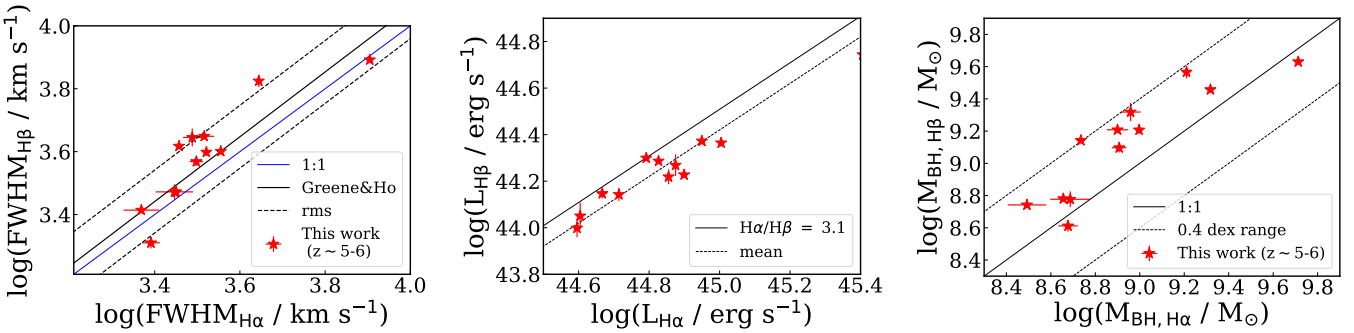

Figure 5. Left: Hα FWHM versus Hβ FWHM. The blue line indicates the 1-to-1 equality. The black solid and dotted lines indicate the best-fit relation of z<0.35 SDSS quasars and the associated 0.1 dex rms from Greene & Ho (2005). **Middle:** Hα luminosity versus Hβ luminosity. The solid line indicates the theoretical expectation of 3.1 and the dotted line indicates the mean value of our sample (3.8). **Right:** BH mass based on Hα and Hβ. The errorbars only reflect the measurement errors. The solid and dotted lines indicate the 1-to-1 equality and the ±0.4 dex ranges, respectively. Overall, the relative Hα and Hβ properties of our sample are consistent with those observed in low-z quasars.

tical to that of the z≤0.35 SDSS quasars (Greene & Ho 2005) and that found in nearby quasars by an even earlier study (Osterbrock & Shuder 1982). It indicates that the FWHM$_{H\beta}$/FWHM$_{H\alpha}$ ratio does not vary in quasars across a large dynamical range of luminosities and redshifts.

The relation between the Hα and Hβ luminosities of our sample is shown in the middle panel of Fig. 5. The mean Hα/Hβ ratio is ∼3.8 (for the combined broad and narrow components; The ratio for the broad component alone is ∼3.9). This ratio is close to that (∼3.5) of the aforementioned z≤0.35 SDSS quasars and that of the value seen in the SDSS quasar composite spectrum from Vanden Berk et al. (2001), and only mildly larger than the theoretical limit of 3.1 (Osterbrock & Ferland 2006). This again suggests strong similarities of the BLR in these quasars, despite their significant differences in luminosities and cosmic epochs. This also suggests that there is little dust extinction in the nuclear region along the line-of-sight of our objects as expected.

The comparison of BH masses derived from Hα and Hβ is shown in the right panel of Fig. 5. Overall, the two BH mass estimators broadly agree with each other. On average, the Hα-based BH mass is slightly lower (∼0.2 dex) than the Hβ-based ones, and the maximum difference is ∼0.4 dex, which is consistent with the findings from previous studies on individual z>6 quasars (Marshall et al. 2023; Loiacono et al. 2024). Such a difference is smaller than the typical statistical uncertainties of Hβ-based BH mass (∼0.5 dex). Unconstrained systematic uncertainties of both BH mass determinations may contribute to this overall offset, which needs to be investigated with larger samples in future studies.

4.3. [O III] *Strength and Kinematics*

[O III] is detected in 16/27 objects (the decrease of BIC, ΔBIC > 0), whereas the remaining 11 objects do not require [O III] in their best-fit model (ΔBIC ≤ 0). The EW$_{[OIII]}$ of our sample spans more than two orders of magnitude, while the bolometric luminosities span merely one order of magnitude. In Liu et al. (2025), we reported a higher frequency of extremely fast [O III] outflows in our sample when compared to that in lower-redshift quasars. Here we further explore the [O III] strength and kinematics of our objects with [O III] detections (The [O III] kinematics were reported in Liu et al. 2025).

While many of our objects follow the "Baldwin effect" where EW$_{[OIII]}$ decreases with increasing bolometric luminosity, there is an exceptional group of objects exhibiting excesses of EW$_{[OIII]}$ (left panel of Fig. 6). Similarly, EW$_{[OIII]}$ also in general decreases with increasing Eddington ratios (e.g., Shen & Ho 2014) in low-z quasars. Again, while most objects fall within this general trend, a few exceptions with elevated EW$_{[OIII]}$ are still seen in our sample (right panel of Fig. 6). Nevertheless, the EW$_{[OIII]}$ boost in them are less prominent compared to the former case. In both cases, the objects with large EW$_{[OIII]}$ usually show highly blueshifted [O III] profiles (large $|v_{98}|$; v_{98} is the velocity where 98% of the [O III] line flux are redshifted with respect to it). For our sample and the *Shen quasars* combined, there is a positive trend between EW$_{[OIII]}$ and $|v_{98}|$ and W$_{90}$ (the line width enclosing 90% of the total line flux) in logarithm, with Pearson correlation coefficients of 0.49 and 0.41 (where ±1 indicate perfect linear correlations and 0 indicates no correlation), and p-values of 2×10^{-4} and 3×10^{-3} (with a null-hypothesis that the two variables are uncorrelated), respectively. On the other hand,

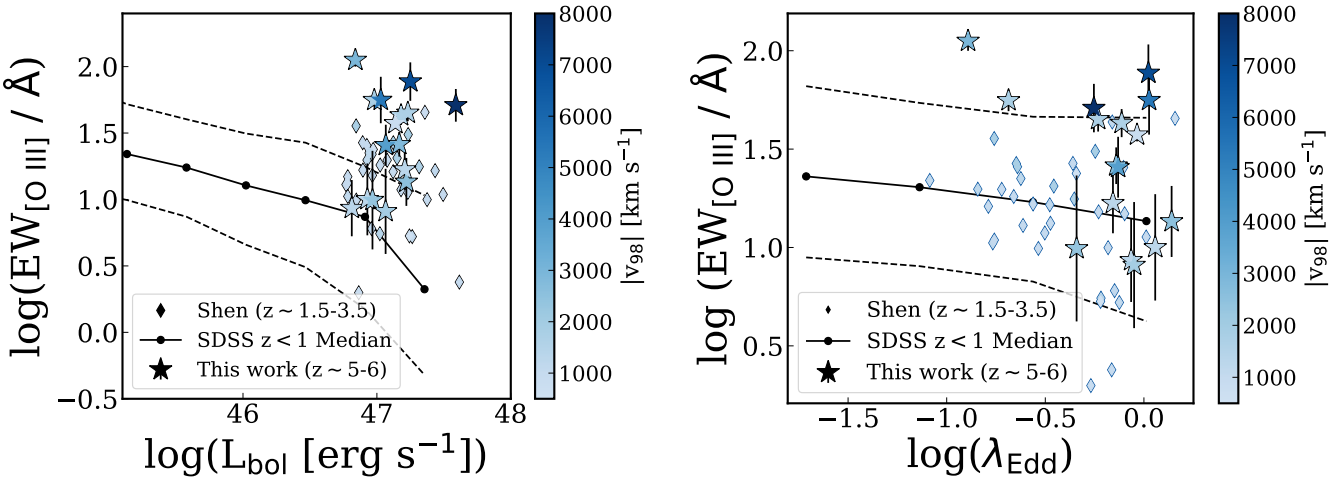

Figure 6. [O III] EW as a function of bolometric luminosity (left), and Eddington ratio (right) for our objects (stars) and *Shen quasars* (diamonds). They are color-coded by the v_{98} of their [O III] emission lines. The median and 16th and 84th percentiles of z<1 SDSS quasars are indicated by the black line with dots and dashed lines, respectively.

for our sample and the *Shen quasars* combined, the dependence of $EW_{[OIII]}$ on the bolometric luminosities, BH mass and Eddington ratios, if any, are quite weak (with Pearson correlation coefficients of 0.007, 0.12, and −0.11). To summarize, the boosted $EW_{[OIII]}$ in our objects is primarily related to the emission from the fast outflows.

4.4. *Eigenvector 1 Relations*

Previous studies suggest that lower-z quasars ($z \lesssim 3$) follow well-defined correlations despite a diverse range of spectroscopic properties. The most prominent one of these correlations, known as "Eigenvector 1 (EV1)", links many quasar properties to the strength of the optical Fe II and [O III] emission. It is widely believed that the main driver of EV1 is the Eddington ratio, and more recently, orientation has also been suggested to play a role in the diversity of quasar phenomenology (Boroson & Green 1992; Boroson 2002; Marziani et al. 2001, 2003; Shen & Ho 2014). In Fig. 7, we examine the locations of our high-z quasar sample in the EV1 planes, namely the correlations of $EW_{[OIII]}$ and $FWHM_{H\beta}$ with R_{Fe}, and compare them with lower-z quasars. Here R_{Fe} is the ratio of EW_{FeII} over $EW_{H\beta,broad}$, where EW_{FeII} is measured between rest-frame 4434 Å and 4684 Å. The two lower-z quasar samples are the z ∼ 1.5−3.5 *Shen quasars* which are matched in bolometric luminosity and all SDSS z<1 quasars from Wu et al. (2023). For objects with no [O III] detections, their $EW_{[OIII]}$ upper limits depend on the assumed [O III] line width, which can vary a lot (as is the case in our sample) and thus make the $EW_{[OIII]}$ upper limits very uncertain. Therefore, in the following analysis related to $EW_{[OIII]}$, we only consider objects with [O III] detections.

Within their small bolometric luminousity range (∼1 dex), our objects shows a broad range of Fe strength, with R_{Fe} range from undetected to ∼2.5. For the two-dimensional EV1 plane of R_{Fe} versus $FWHM_{H\beta}$, all but one of our objects fall within/close to the 99% contours of z<1 SDSS quasars. This is consistent with previous studies of z>6.5 quasars (Yang et al. 2023). The only exception in our sample shows larger R_{Fe} given its $FWHM_{H\beta}$ which is rare but not unseen in z<1 SDSS quasars and cosmic noon *Shen quasars*. The median $FWHM_{H\beta}$ of our sample (∼3600 km s^{-1}) is smaller than that of *Shen quasars* (∼ 5000 km s^{-1}), consistent with our findings from the composite spectrum (Fig. 3). Meanwhile, it should be noted that at fixed R_{Fe}, the dispersion in $FWHM_{H\beta}$ could be dominated by the orientation effect (e.g., Shen & Ho 2014). Therefore, the lower $FWHM_{H\beta}$ in our sample may be partly caused by a combination of the orientation effect and small sample size.

For the EV1 plane of $EW_{[OIII]}$ versus R_{Fe}, all but three objects in our sample show $EW_{[OIII]}$ falling within the 10%–90% range of SDSS z<1 quasars. The three objects beyond the 10%–90% SDSS range show significantly larger $EW_{[OIII]}$ than the *Shen quasars*. At the same bolometric luminosity range, while the overall detection rates of [O III] emission line in our sample and the *Shen quasars* are similar (∼60% with S/N > 3), the median $EW_{[OIII]}$ of these detections in our sample (∼32 Å) is larger than those of *Shen quasars* (∼16 Å).

The 3 outliers with large $EW_{[OIII]}$ in our sample, J0759+1800, J1141+7119, and J1620+5202, have

Table 2. Sample Properties

Object	$\log(L_{\rm bol})$	$\rm EW_{[OIII]}$	$\rm R_{Fe}$	$\log(L_{\rm H\beta})$	$\rm FWHM_{H\beta}$	$\log(\rm M_{BH})$	$\lambda_{\rm Edd}$	$\log(L_{\rm H\alpha})$	$\rm FWHM_{H\alpha}$	$\log(\rm M_{BH,H\alpha})$
	[erg s^{-1}]	[Å]		[erg s^{-1}]	[km s^{-1}]	[$\rm M_\odot$]		[erg s^{-1}]	[km s^{-1}]	[$\rm M_\odot$]
(1)	(2)	(3)	(4)	(5)	(6)	(7)	(8)	(9)	(10)	(11)
J0732+3256	47.5	-	2.37±0.03	44.53±0.01	3570±82	9.29±0.02	1.34±0.07	-	-	-
J0756+0218	46.8	-	2.29±0.06	44.00±0.04	2966±59	8.78±0.02	0.87±0.05	44.60±0.01	2820±56	8.66±0.02
J0759+1800	47.2	77.1±25.7	1.26±0.02	44.87±0.03	3448±398	9.13±0.10	1.05±0.38	-	-	-
J0807+1328	47.2	16.8±5.9	1.56±0.05	44.57±0.02	4139±83	9.26±0.02	0.70±0.04	-	-	-
J0829+0303	47.1	25.6±9.1	0.84±0.03	44.27±0.05	3702±123	9.10±0.03	0.74±0.06	44.88±0.01	3145±113	8.91±0.03
J0831+4046	47.2	-	1.35±0.07	44.24±0.05	2548±51	8.83±0.02	1.79±0.09	-	-	-
J0840+5624	47.2	26.0±5.6	0.99±0.02	44.37±0.01	3968±110	9.21±0.02	0.72±0.05	44.95±0.01	3320±66	9.00±0.02
J0850+3246	47.2	-	1.41±0.03	44.33±0.02	4418±290	9.32±0.06	0.61±0.10	45.00±0.01	3077±151	8.96±0.04
J0859+2520	47.0	56.0±22.6	0.50±0.01	44.74±0.01	3024±169	8.90±0.05	1.06±0.15	-	-	-
J0927+2001	47.0	-	2.22±0.04	44.14±0.03	4145±83	9.14±0.02	0.52±0.03	44.71±0.01	2864±57	8.74±0.02
J0941+5947	47.2	13.6±5.6	0.67±0.03	44.73±0.02	2960±59	8.98±0.02	1.38±0.07	-	-	-
J0953+6910	47.0	-	1.30±0.05	44.05±0.06	2594±52	8.74±0.02	1.36±0.07	44.60±0.01	2336±226	8.49±0.09
J1050+4627	47.1	37.4±2.9	<1.08	44.41±0.02	3455±69	9.07±0.02	0.92±0.04	-	-	-
J1100+5800	47.2	42.9±7.0	0.41±0.01	44.70±0.01	3873±77	9.19±0.02	0.77±0.04	-	-	-
J1102+6635	46.9	-	0.51±0.08	44.23±0.10	3424±632	8.95±0.16	0.73±0.61	-	-	-
J1116+5853	46.8	8.6±4.2	0.92±0.04	44.15±0.02	2965±167	8.78±0.05	0.86±0.13	44.67±0.01	2795±282	8.69±0.09
J1134+3928	46.8	-	1.74±0.08	44.18±0.05	3702±74	8.95±0.02	0.53±0.04	-	-	-
J1141+7119	46.8	112.1±12.9	1.77±0.09	44.28±0.01	7800±156	9.63±0.02	0.13±0.01	44.81±0.01	8031±161	9.71±0.02
J1245+4348	47.3	-	0.78±0.02	44.65±0.02	2820±79	8.99±0.02	1.71±0.12	-	-	-
J1257+6349	47.1	-	1.36±0.03	44.22±0.03	2042±83	8.61±0.04	2.62±0.26	44.86±0.01	2462±119	8.68±0.04
J1327+5732	47.0	55.9±7.0	<0.69	44.20±0.01	6680±301	9.57±0.04	0.21±0.02	44.88±0.01	4408±88	9.21±0.02
J1328+4445	47.2	44.8±6.4	<0.55	44.68±0.02	4574±271	9.36±0.05	0.59±0.09	-	-	-
J1342+5838	46.9	10.0±6.2	0.71±0.04	44.29±0.03	2754±536	8.77±0.17	1.14±1.06	-	-	-
J1436+5007	47.0	9.9±8.4	0.99±0.03	44.30±0.01	4455±89	9.21±0.02	0.46±0.02	44.79±0.01	3282±174	8.90±0.05
J1458+3327	47.1	8.1±6.0	1.04±0.04	44.37±0.03	3370±584	9.01±0.15	0.89±0.65	-	-	-
J1620+5202	47.6	51.1±14.5	1.19±0.04	44.82±0.01	5763±115	9.74±0.02	0.56±0.03	-	-	-
J1621+5155	47.7	-	0.35±0.01	44.74±0.01	3990±80	9.46±0.02	1.26±0.06	45.41±0.01	3590±72	9.32±0.02

NOTE—(2): quasar bolometric luminosity determined from the 5100 Å continuum luminosity. (3): rest-frame equivalent width of [O III] λ5007. (4): Fe strength, defined as the ratio of $\rm EW_{FeII}$ over $\rm EW_{H\beta,broad}$. (5)–(8): Hβ luminosity, FWHM, BH mass and Eddington ratio. (9)–(11): Hα luminosity, FWHM and BH mass. Only the measurement errors are reported.

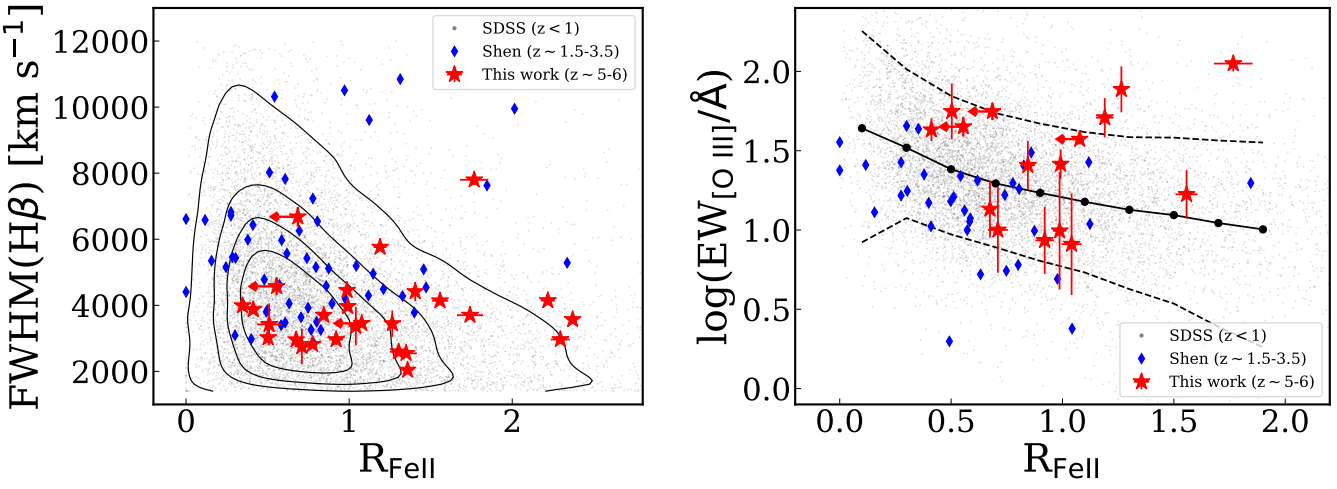

Figure 7. Eigenvector 1 planes defined by broad Hβ FWHM versus $\rm R_{Fe}$ (left) and [O III] EW versus $\rm R_{Fe}$ (right) for our sample (red stars), *Shen quasars* (blue diamonds), and SDSS z<1 quasars (gray dots). In the left panel, the contours correspond to the 99%, 90%, 75% and 50% percentiles of the the distribution of the SDSS sample. In the right panel, the solid and dashed lines indicate the median, 10th and 90th percentiles of the distribution of the SDSS sample.

prominent, blueshifted [O III] emission line tracing fast outflows that are among the fastest ones in our sample. This is again in line with the findings shown in Fig. 6 and Sec. 4.3, where there is a positive trend between $EW_{[OIII]}$ and [O III] outflow velocity in our sample. This reinforces the picture that the boost of [O III] strength some objects within our sample is caused by the presence of fast [O III] outflows (Liu et al. 2025). On the other hand, the systematically lower $EW_{[OIII]}$ observed in the *Shen quasars* than in the z<1 SDSS quasars, can be explained well by the "Baldwin effect" as the mean luminosity of *Shen quasars* is higher than the whole population of z<1 SDSS quasars.

Moreover, the R_{Fe} itself may also be taken as a crude indicator of the metallicity of the BLR. Our sample exhibits a R_{Fe} range similar to that of z<1 SDSS quasars, suggesting that the BLR of our z ∼ 5–6 quasars already has metallicity comparable to those of nearby quasars. In our sample, 3 objects show R_{Fe} larger than 99% of low-z SDSS quasars at a given $FWHM_{H\beta}$. Additionally, 20 out of our 27 objects show $R_{Fe} > 0.6$, the value corresponds to solar metallicity as found in a previous study (Netzer & Trakhtenbrot 2007). These may imply super-solar metallicty in the BLR of a significant portion of our high-z quasars and a very short time scale of metal enrichment in them.

Overall, most object in our z ∼ 5–6 sample fall within the EV1 planes formed by the low-z quasars. These high-z luminous quasars likely possess BLR/NLR as mature as their low-z siblings, despite the much more limited evolution time available for the former. In addition, our high-z sample contains a population of sources with significantly stronger, more blueshifted and broader [O III] line emission than those of low-z quasars, which is due to the presence of fast galaxy-scale outflows in those systems.

5. SPATIALLY EXTENDED EMISSION

We first look for dual/binary quasars and lensed quasars in our sample. Among the 27 objects, we see no evidence of dual/binary quasars or lensed quasars. This is consistent with the low detection rates of them at $z \gtrsim 5$ where only a few objects have been reported in the literature so far (e.g., Fan et al. 2019; Yue et al. 2023; Matsuoka et al. 2024)

Our IFU data also provide a glance at the extended line emission from the quasar host galaxy and/or companion galaxy within our sample, which unveils the gaseous environments they live in (e.g., Veilleux et al. 2023; Liu et al. 2024, 2025). We apply a simple PSF subtraction by first constructing a 2D PSF model using the flux map of the broad Hβ emission line wing within the velocity range of [−1500,−500] and [+500, +1500] km s^{-1}, which relies on the fact that the broad Hβ emission comes from the spatially unresolved BLR of the quasar. Next, we extract a "pure" quasar spectrum from the spaxel with the maximum wavelength-integrated total flux (i.e., the spaxel where the quasar is located). Finally, we scale-down the flux level of the "pure" quasar spectrum adopting the value of the PSF model at each spaxel and subtract it from the spectrum of the same spaxel, which gives the final PSF-subtracted spectrum for that spaxel.

We see clear evidence of extended [O III] line emission from the host galaxy and/or companion galaxy in 6 objects, J0807+1328, J0840+5624, J1050+4627, J1141+7119 J1327+5732, and J1328+4445, which gives a detection rate of 6/27 or ∼22% in our sample. This incidence rate should be treated as a lower limit since i) more diffuse, fainter emission will be missed by our shallow observation (only ∼8 min exposures, ∼1–5% of other NIRSpec/IFU programs targeting individual high-z quasar) and ii) our PSF subtraction assumes that the brightest spaxel is pure quasar emission, which may still be contaminated by host galaxy emission in reality and could thus result in an oversubtraction of the quasar PSF. The PSF-subtracted, moment 0 (flux), moment 1 (velocity), and moment 2 (velocity dispersion) maps of [O III] λ5007 of the 6 objects are shown in Fig. 8 and 9. They are calculated over the [−1000, +1000] km s^{-1} range that is wide enough for our objects after the PSF subtraction. The extended line emission shows asymmetric morphologies in all 6 objects, although the evidence in J1050+4627 and J1328+4456 is weak. The velocities (moment 1) of these extended [O III] emission are in general modest, mostly within ±300 km s^{-1} from the systemic velocities. The velocity dispersions (moment 2) of them range from ∼200 to ∼500 km s^{-1}. These characteristics may be consistent with late-stage merging activities within these systems, implying frequent merger events in these z ∼ 5–6 quasars. Nevertheless, [O III] emission is tracing ionized gas rather than stellar components within these systems. As a result, these [O III] emissions may alternatively trace the turbulent and/or clumpy interstellar medium of these quasar host galaxies. While [O III] outflows are detected in the integrated spectra of all these 6 objects (Liu et al. 2025), our shallow observation could not unambiguously unveil the extended outflows in most of these objects, which are traced by faint broad emission line wings. Nevertheless, as demonstrated in Liu et al. (2025), the blueshifted [O III] line emission in J1141+7119 is extended up to ∼2 kpc, confirming that the outflow is on galaxy-scale (kpc-scale). Consistently, the moment 1 map of this

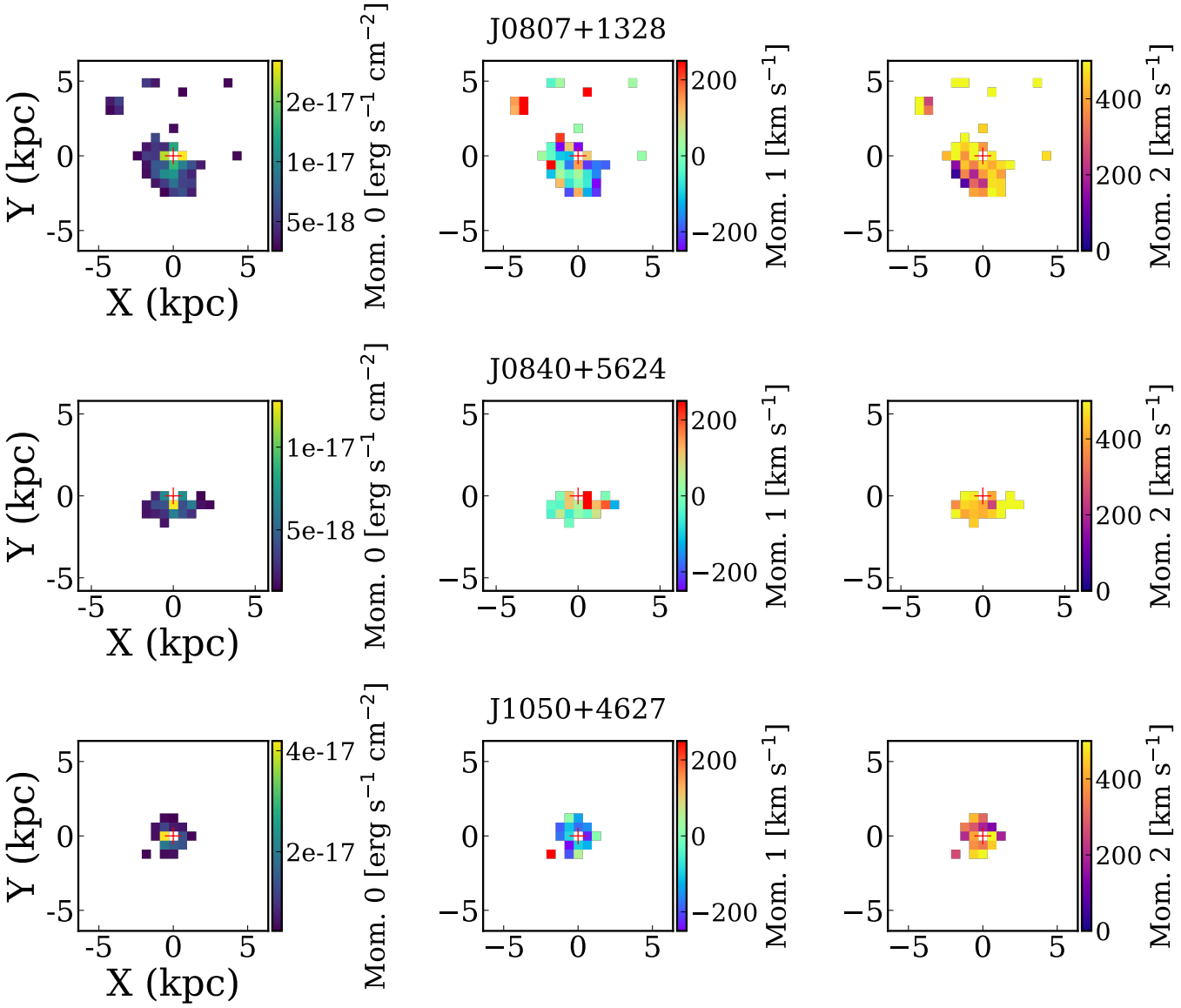

Figure 8. PSF-subtracted IFU maps for the first 3 of the 6 objects with clear extended [O III] line emission. For each object, moment 0 (flux) , moment 1 (velocity) and moment 2 (velocity dispersion) are shown from left to right. Spaxels with S/N < 5 are omitted from the maps.

object is dominated by spaxels with blueshifts, even though the moment 1 itself is insensitive to the faint, broad emission line wing tracing the outflow. Similar extended line emission properties are also reported from deeper IFU observations of other individual high-z quasars, tracing merging activity, companion galaxies and/or outflows (e.g. Decarli et al. 2024; Liu et al. 2024; Marshall et al. 2023, 2024, 2025). In all, these high-z quasars in our sample likely live in busy close environments with frequent mergers. Future deeper JWST NIRSpec/IFU data combined with more detailed quasar PSF subtraction are needed to better decipher the extended line emission in these objects and reveal more potential fainter extended emission in the rest of the sample.

5.1. *J1327+5732*

The most extended [O III] line emission is seen in J1327+5732, which extends up to ∼5 kpc (the middle row of Fig. 9). A tentative negative-positive velocity gradient is visible in the vicinity of the quasar, which may trace the rotating gas within the quasar host galaxy. There is a distinct line-emitting region east of the quasar (marked in Fig. 9; denoted as J1327_E hereafter), with a clear luminosity centroid ∼2.5 kpc from the quasar and S/N ([O III]) > 10 for all spaxels within 0.2″ (∼1.2 kpc) from the centroid. It has modest velocities (< ±200 km

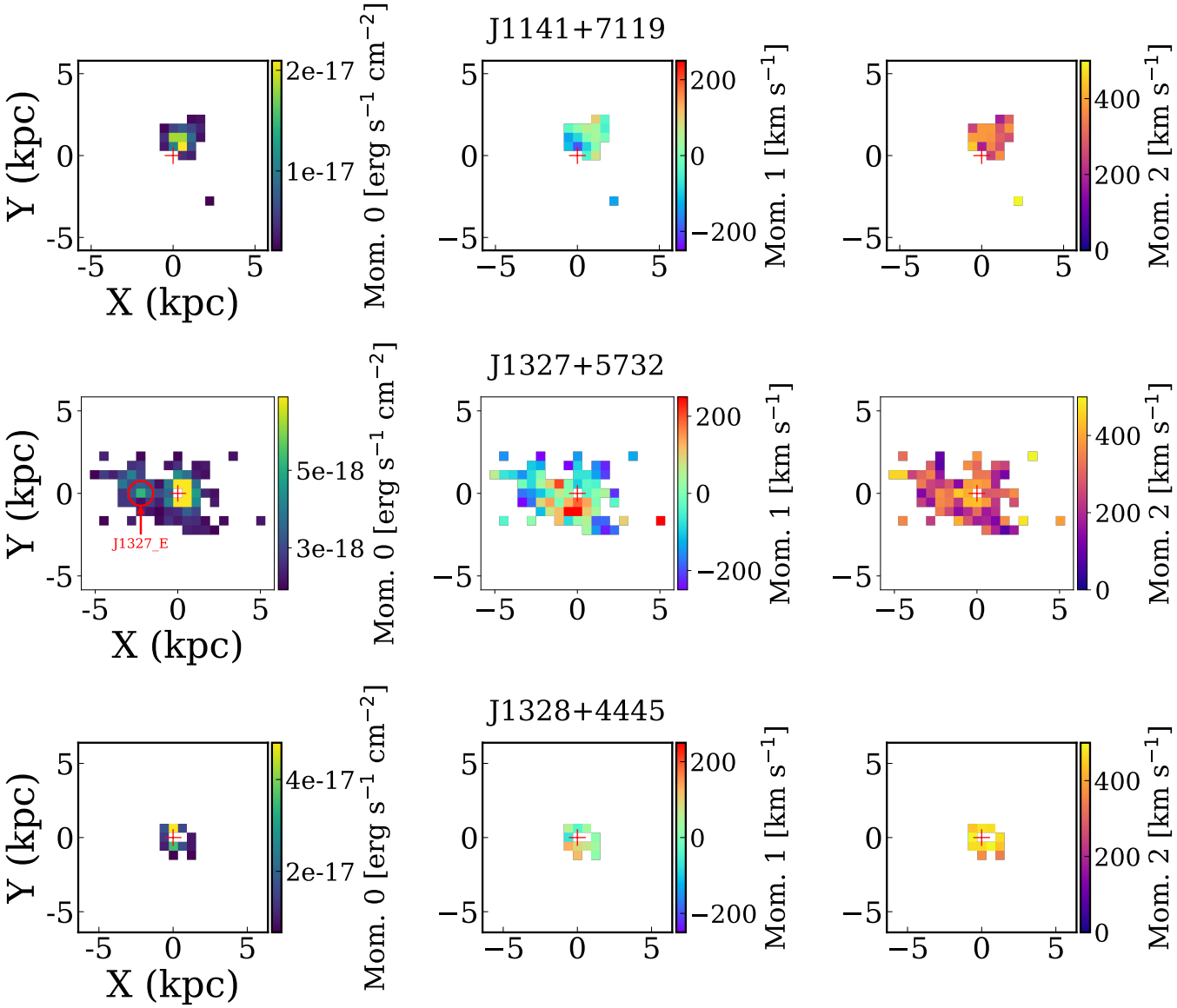

Figure 9. Same as Fig. 8 but for the remaining 3 objects. For J1327+5732, the red circle indicates the aperture to extract the spectrum for the merging companion J1327_E. See Sec. 5.1 for details.

s^{-1}) and velocity dispersions (<200 km s^{-1}). The integrated spectrum of J1327_E extracted from an aperture with 0.2″ radius from the quasar PSF-subtracted data cube is shown in Fig. 10, where major emission lines including [O III] $\lambda\lambda$4959,5007, [N II] $\lambda\lambda$6548,6583 and Hα are detected. We fit the emission line profiles of all major emission lines detected with a single Gaussian profile adopting the same kinematics (i.e., velocity and velocity dispersion). The emission lines show small blueshift (~ -20 km s^{-1}) and are narrow ($\sim$ 140 km s^{-1}), and we see no evidence of broad Hα emission lines tracing AGN activity in our spectrum. We obtain an observed [O III] luminosity of $\sim(5.8 \pm 0.2)\times10^{42}$ erg s^{-1} and Hα luminosity of $\sim(2.1 \pm 0.3)\times10^{42}$ erg s^{-1}, without dust-extinction correction. These are comparable to those found for star-forming galaxies near quasars at z $\sim$ 6 (e.g., Wang et al. 2023; Champagne et al. 2025; Decarli et al. 2024; Marshall et al. 2023, 2024, 2025).

Based on all these observational evidence above, J1327_E is most likely a companion galaxy that is merging with the quasar host galaxy. This serves as an example of how a quasar host galaxy at z $\sim$ 6 is rapidly building up by accreting companion sources. However, we cannot formally rule out the possibility that it traces a very luminous ionized gas clumps within the quasar host galaxy itself. In the following discussions, we assume that J1327_E is indeed a companion galaxy in the process of merging with the quasar host galaxy.

The location of J1327_E on the BPT diagram (Baldwin et al. 1981) is shown in the right panel of Fig. 10. The 3-σ upper limit of the Hβ luminosity is adopted to derive the lower limit for the [O III]/Hβ ratio. J1327_E is located in the AGN area (i.e, above the maximum starburst line) defined for galaxies in the low-z universe (Kewley et al. 2001; Kauffmann et al. 2003). It is still in the AGN region when considering the modified AGN vs star-forming galaxy dividing line at z>3 as defined in Scholtz et al. (2023), where the shift of the dividing line is mainly caused by the low metallicity of high-z AGN.

It has been observed in other systems that a central quasar/AGN may photoionize nearby companion galaxies (e.g., Moran et al. 1992; da Silva et al. 2011; Merluzzi et al. 2018; Keel et al. 2019; Moiseev et al. 2023; Protušová et al. 2024; Marshall et al. 2025), which are also seen in some simulations (e.g., Costa et al. 2014; Chen 2020). Similar to the approach presented in Sec. 6.4 of Marshall et al. (2025), we estimate whether the quasar is luminous enough to ionize the gas within J1327_E. The ionizing photon rate required to generate the observed Hα luminosity of J1327_E is

$$Q_{\rm ionizing} = L_{\rm H\alpha}/(1.4\times10^{-12}\,{\rm erg}) \quad , \tag{3}$$

assuming that one Hα photon is produced for every 2.98 recombinations (Hummer & Storey 1987). This leads to an incident ionizing-photon rate of $Q_{\rm ionizing} \simeq 1.5\times10^{54}\,{\rm s^{-1}}$.

The incident ionizing quasar luminosity onto J1327_E is

$$L_{\rm incident} = L_{\rm bol}\gamma\frac{\Omega}{4\pi} \quad , \tag{4}$$

where γ is the ratio of ionizing to bolometric luminosity, and Ω is the solid angle the companion subtends as seen from the quasar. For small angles, $\Omega \simeq \pi(\arctan{(r/d)})^2$. For a typical type 1 quasar, $\gamma = 0.14$ (Keel et al. 2019). The size r is estimated as the extent of the [O III] emission of J1327_E perpendicular to the direction of the quasar on the sky plane, which gives $r = 0\farcs2$. The distance d is calculated from the luminosity centroid of J1327_E to the quasar. The ionizing luminosity is further converted to the incident photon rate adopting a mean ionizing photon energy of 2 rydbergs or 4.36×10^{-11} erg. Therefore,

$$Q_{\rm incident} = L_{\rm incident}/(4.36\times10^{-11}\,{\rm erg}) \quad . \tag{5}$$

This gives $Q_{\rm incident} \simeq 5.5\times10^{54}\,{\rm s^{-1}}$. The incident photon rate from the quasar is thus sufficient to photoionize J1327_E, with $Q_{\rm incident}/Q_{\rm ionizing} \simeq 3.6$. We note that there are several caveats associated with our estimation: i) The distance between J1327_E and the quasar is not de-projected. The physical distance could be larger and require higher ionizing luminosity from the quasar. ii) The Hα luminosity is not dust extinction corrected, which will also require higher quasar ionizing luminosity. iii) The quasar could be more luminous in the past and has now faded, as seen for Hanny's Voorwerp and other AGN-ionized clouds on timescales of $\sim10^4$–10^5 yr. (Lintott et al. 2009; Schawinski et al. 2010; Keel et al. 2012a,b; Schirmer et al. 2013). This will give a higher quasar ionizing luminosity than currently observed.

Overall, our calculation suggests that the quasar, in principle, has enough ionizing photons to photoionize the gas within J1327_E, which naturally explains that J1327_E is in the AGN region of the BPT diagram. This provides tentative evidence that quasar radiative feedback may be capable of shaping the physical properties of the gas within the merging companion galaxies. Similar radiative feedback but on larger spatial scales is also speculated for a luminous z $\sim$ 6 quasar (Zhu et al. 2025). Nevertheless, this does not rule out the possibility that J1327_E hosts an AGN within itself. Future deeper JWST/NIRSpec and/or JWST/MIRI observations could better diagnose the existence of an AGN within J1327_E through broad emission lines and/or AGN torus emission. If confirmed, this system, to our knowledge, will be the first close quasar-AGN pair reported at this redshift, adding another intriguing example of kpc-scale dual AGN in the early universe (e.g., Maiolino et al. 2024; Li et al. 2025).

6. CONCLUSION

In this paper, we present the results from our JWST survey program (Q-IFU) of 27 luminous quasars at $z\sim$ 4.74 - 4.88 and $z\sim$ 5.66 – 6 with NIRSpec/IFU. We derive and analyze rest-frame optical nuclear properties of these quasars and extended line emission within these systems for the first time. Our main findings are summarized below.

- We determine the systemic redshifts of our objects through the peak of the narrow [O III] component or the overall Hβ component when no narrow [O III] emission line is detected. Our mean and median redshifts $\sim$390 and $\sim$40 km s^{-1} larger than the rest-frame UV emission line-based redshifts (including C IV, C III] and/or Si IV]) in the literature, respectively, despite the large scatter.

- We build a composite spectrum for our whole sample with median combining, which is overall similar to that of *Shen quasars* at z $\sim$ 1.5–3.5 sharing the same bolometric luminosity range as our sample. The most obvious difference lies in the [O III] line emission which is more blueshifted and

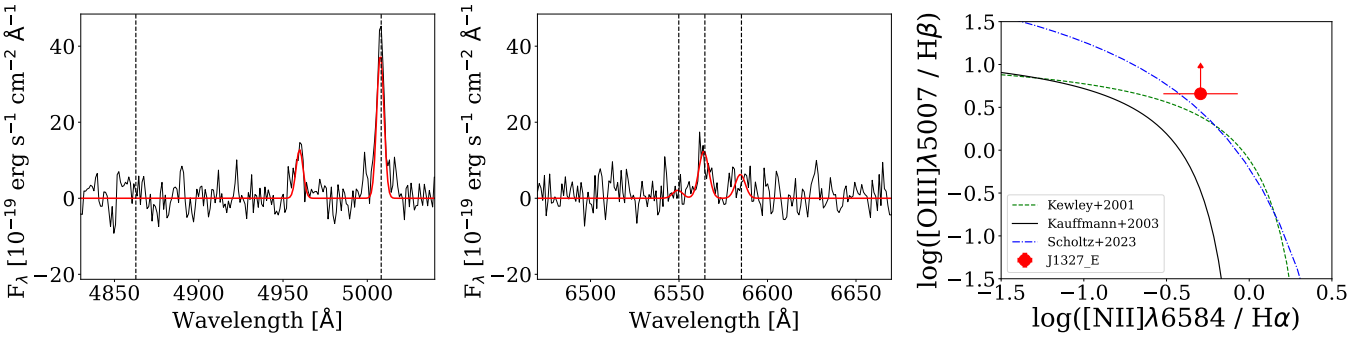

Figure 10. Left and Middle: Zoom-in spectra and best-fit models for Hβ (undetected), [O III] $\lambda\lambda$4959,5007, [N II] $\lambda\lambda$6548,6583 and Hα emission lines for J1327_E. The location of each emission line at the quasar systemic velocity is indicated by the dashed line. **Right:** The location of J1327_E on the BPT diagram. The black and green dashed line indicate the AGN versus star-forming galaxies for low-z objects as defined in Kauffmann et al. (2003) and Kewley et al. (2001), respectively. The blue dash-dotted line indicates the new dividing line defined for high-z objects based on JWST results from Scholtz et al. (2023).

broader yet weaker in our sample when compared to the *Shen quasars*. This is consistent with the enhanced frequency of extremely fast outflows in our sample as reported in Liu et al. (2025). In addition, while the differences are more subtle with respect to the case of [O III] the Balmer emission lines are broader and the Fe emission is stronger in our sample.

- We obtain bolometric luminosities of log(L_{bol}/erg s^{-1}) $\sim$ 46.8–47.7, Hβ-based BH masses of log($M_{BH}/M_\odot$) $\sim$ 8.6–9.7 and Eddington ratios of $\sim$ 0.1–2.6 for our sample. Our results confirm that these luminous quasars are powered by actively accreting, $\sim10^9$ $M_\odot$ BH holes within $\sim$1 Gyr after the Big Bang. Comparing to the *Shen quasars* at z $\sim$ 1.5–3.5 within the same bolometric luminosity range, our sample shows larger median BH mass (9.10 vs 9.32) and Eddington ratio (0.86 vs 0.44). Nevertheless, such a difference may be insignificant as the 90% confidence levels of the median BH mass are 8.90–9.31 vs 9.22–9.51, and those of median Eddington ratios are 0.48—1.25 vs 0.28—0.54. In addition, for the two objects in our sample with Mg II-based BH masses in the literature, our Hβ-based BH masses agree with the Mg II-based values.

- The Hα emission lines are covered for 12 objects. The FWHM of Hβ and Hα lines agree with each other well and fall within the $\sim$0.1 dex rms scatter of a low-z study (z$\leq$0.35). The mean Hα/Hβ ratio is $\sim$3.8, close to the value ($\sim$3.5) obtained from the aforementioned low-z study of luminous quasars and the theoretical limit of 3.1. The Hβ-based and Hα-based BH masses are broadly consistent with each other, despite a potential small average offset of $\sim$+0.2 dex and a maximum difference of $\sim$0.4 dex.

- The dependence of $EW_{[OIII]}$ on the quasar luminosities and Eddington ratios in general follow the trends formed by low-z quasars, except that several objects show boosted $EW_{[OIII]}$, especially in the $EW_{[OIII]}$ vs quasar luminosity plane. Our objects also generally fall within the same region as occupied by low-z quasars in the Eigenvector 1 planes. In the $EW_{[OIII]}$ vs R_{Fe} plane, there are three objects with higher $EW_{[OIII]}$ than the general trend. In both cases, the $EW_{[OIII]}$ excess seen in certain objects of our sample are primarily related to the emission from the fast outflows.

- We see no evidence of dual/binary quasars and lensed quasars in our shallow survey. We have uncovered extended line emission in 6 out of the 27 objects after PSF subtraction, which should be deemed as a lower limit given the shallowness of our IFU data. The extended emission shows asymmetric morphologies in all 6 objects to varying degrees, with absolute velocities $\lesssim$300 km s^{-1} and velocity dispersions of $\sim$200–500 km s^{-1}. These characteristics may trace late-stage merger activities, turbulent and clumpy ISM, and/or companion galaxies.

- Among them, J1327+5732 exhibits the most extended line-emitting region (up to $\sim$5 kpc radially). The gas in the vicinity of the quasar shows a velocity gradient potentially tracing gas rotation. We discover a distinct line emitting region, J1327_E, which is $\sim$2.5 kpc away from the quasar and most likely a merging companion galaxy. It is presumably ionized by the quasar radiation, providing tentative evidence of on-going quasar ra-

diative feedback shaping the ISM properties of a merging companion galaxy. Nevertheless, the possibility that there is an AGN within J1327_E itself cannot be ruled out.

ACKNOWLEDGMENTS

WL acknowledges funding from the JWST Arizona/Steward Postdoc in Early galaxies and Reionization (JASPER) Scholar contract at the University of Arizona. W.L. acknowledges support from NASA through STScI grant JWST-Survey-3428. This work is based on observations made with the NASA/ESA/CSA James Webb Space Telescope. The data were obtained from the Mikulski Archive for Space Telescopes at the Space Telescope Science Institute, which is operated by the Association of Universities for Research in Astronomy, Inc., under NASA contract NAS 5-03127 for JWST. These observations are associated with programs #3428. Support for these programs was given through a grant from the Space Telescope Science Institute, which is operated by the Association of Universities for Research in Astronomy, Inc., under NASA contract NAS 5-03127.

AUTHOR CONTRIBUTIONS

W.L. conceived the project, carried out the data reduction and analysis, and wrote the manuscript. He is also the PI of the JWST survey program #3428 where the data come from. X.F. helped revise the manuscript and provided suggestions for data analysis and interpretation. All authors reviewed and/or commented on the manuscript.

APPENDIX

A. SPECTRA AND BEST-FITS OF INDIVIDUAL OBJECTS

The spectra and their best-fits covering the Hγ, Hγ, and [O III] regions of our sample are shown in Fig. 11, except for the 6 objects with the most extreme outflows that are presented in Liu et al. (2025). Those of the Hα regions for the 12 objects with corresponding spectral coverages are shown in Fig. 12.

Facilities: JWST(NIRSpec)

Software: astropy (Astropy Collaboration et al. 2018), PyQSOFit (Guo et al. 2018; Shen et al. 2019)

REFERENCES

Assef, R. J., Denney, K. D., Kochanek, C. S., et al. 2011, ApJ, 742, 93, doi: 10.1088/0004-637X/742/2/93

Astropy Collaboration, Price-Whelan, A. M., Sipőcz, B. M., et al. 2018, AJ, 156, 123, doi: 10.3847/1538-3881/aabc4f

Bañados, E., Venemans, B. P., Mazzucchelli, C., et al. 2018, Nature, 553, 473, doi: 10.1038/nature25180

Baldwin, J. A. 1977, ApJ, 214, 679, doi: 10.1086/155294

Baldwin, J. A., Phillips, M. M., & Terlevich, R. 1981, PASP, 93, 5, doi: 10.1086/130766

Barth, A. J., Bennert, V. N., Canalizo, G., et al. 2015, ApJS, 217, 26, doi: 10.1088/0067-0049/217/2/26

Böker, T., Arribas, S., Lützgendorf, N., et al. 2022, A&A, 661, A82, doi: 10.1051/0004-6361/202142589

Boroson, T. A. 2002, ApJ, 565, 78, doi: 10.1086/324486

Boroson, T. A., & Green, R. F. 1992, ApJS, 80, 109, doi: 10.1086/191661

Brotherton, M. S., Runnoe, J. C., Shang, Z., & DiPompeo, M. A. 2015, MNRAS, 451, 1290, doi: 10.1093/mnras/stv767

Carniani, S., Marconi, A., Maiolino, R., et al. 2015, A&A, 580, A102, doi: 10.1051/0004-6361/201526557

Champagne, J. B., Wang, F., Zhang, H., et al. 2025, ApJ, 981, 113, doi: 10.3847/1538-4357/adb1bd

Chen, H. 2020, ApJ, 893, 165, doi: 10.3847/1538-4357/ab80c6

Costa, T., Sijacki, D., Trenti, M., & Haehnelt, M. G. 2014, MNRAS, 439, 2146, doi: 10.1093/mnras/stu101

da Silva, R. L., Prochaska, J. X., Rosario, D., Tumlinson, J., & Tripp, T. M. 2011, ApJ, 735, 54, doi: 10.1088/0004-637X/735/1/54

Decarli, R., Loiacono, F., Farina, E. P., et al. 2024, A&A, 689, A219, doi: 10.1051/0004-6361/202449239

Dietrich, M., Appenzeller, I., Vestergaard, M., & Wagner, S. J. 2002, ApJ, 564, 581, doi: 10.1086/324337

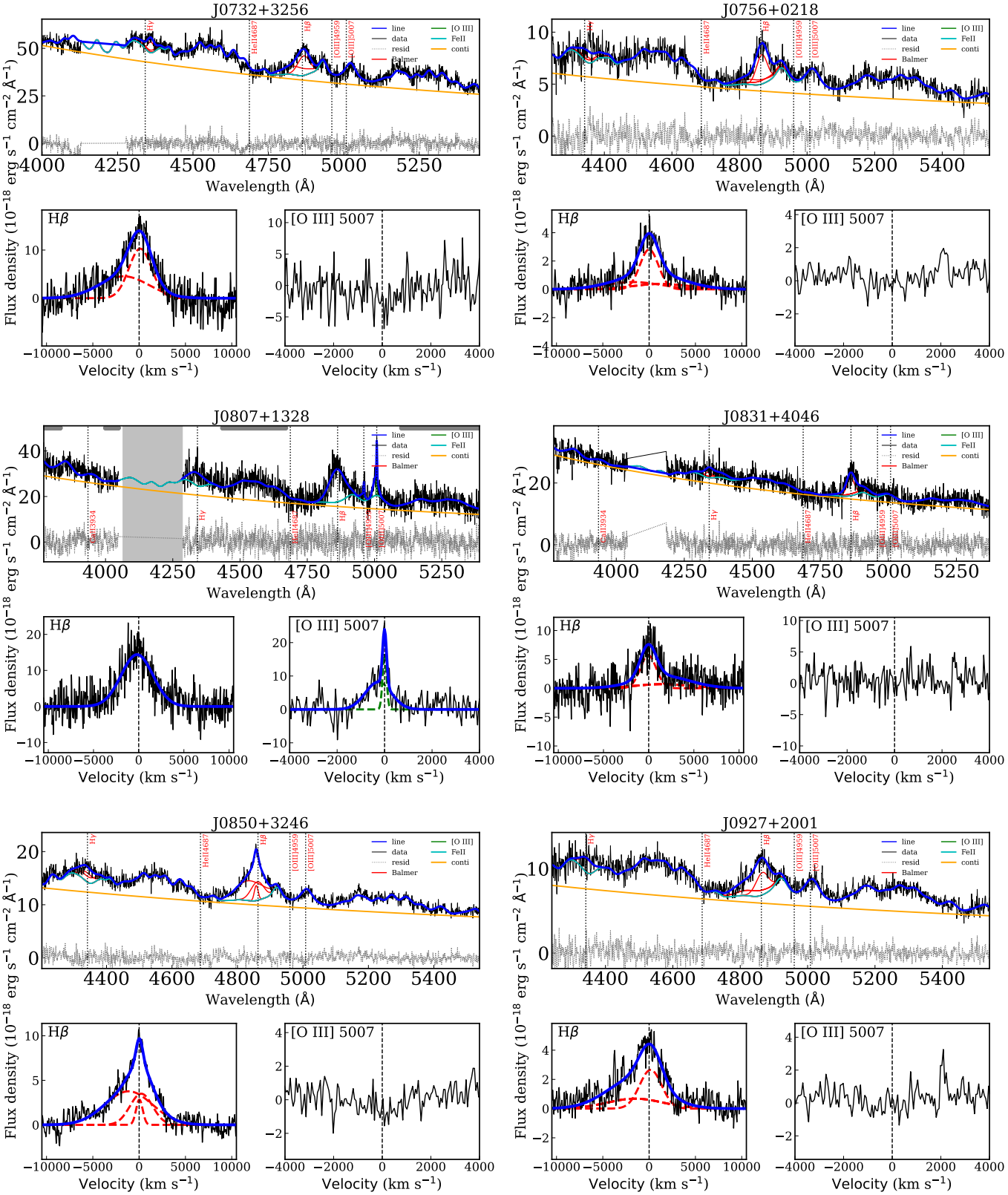

Figure 11. For each frame of an individual object: **Top panel:** JWST spectrum (black), best-fit emission line profiles (blue), Fe emission (cyan), continuum (orange), and residual (gray dotted line). The best-fit individual Gaussian components for Hβ and Hγ are shown in red and those for [O III] $\lambda\lambda$4959,5007 are shown in green. Systemic velocities of individual emission lines are shown in vertical black dotted lines. The spectral windows adopted for fitting the quasar pseudo continuum are marked by the gray thick bars. The detector gap and adjacent noisy regions not used in the fitting are masked by the vertical gray shaded region. **Bottom panels:** Hβ (left) and [O III] λ5007 (right) line profiles with their best-fit models (blue solid lines) and individual components (dashed lines). For [O III], only the residuals are shown when the line is not detected.

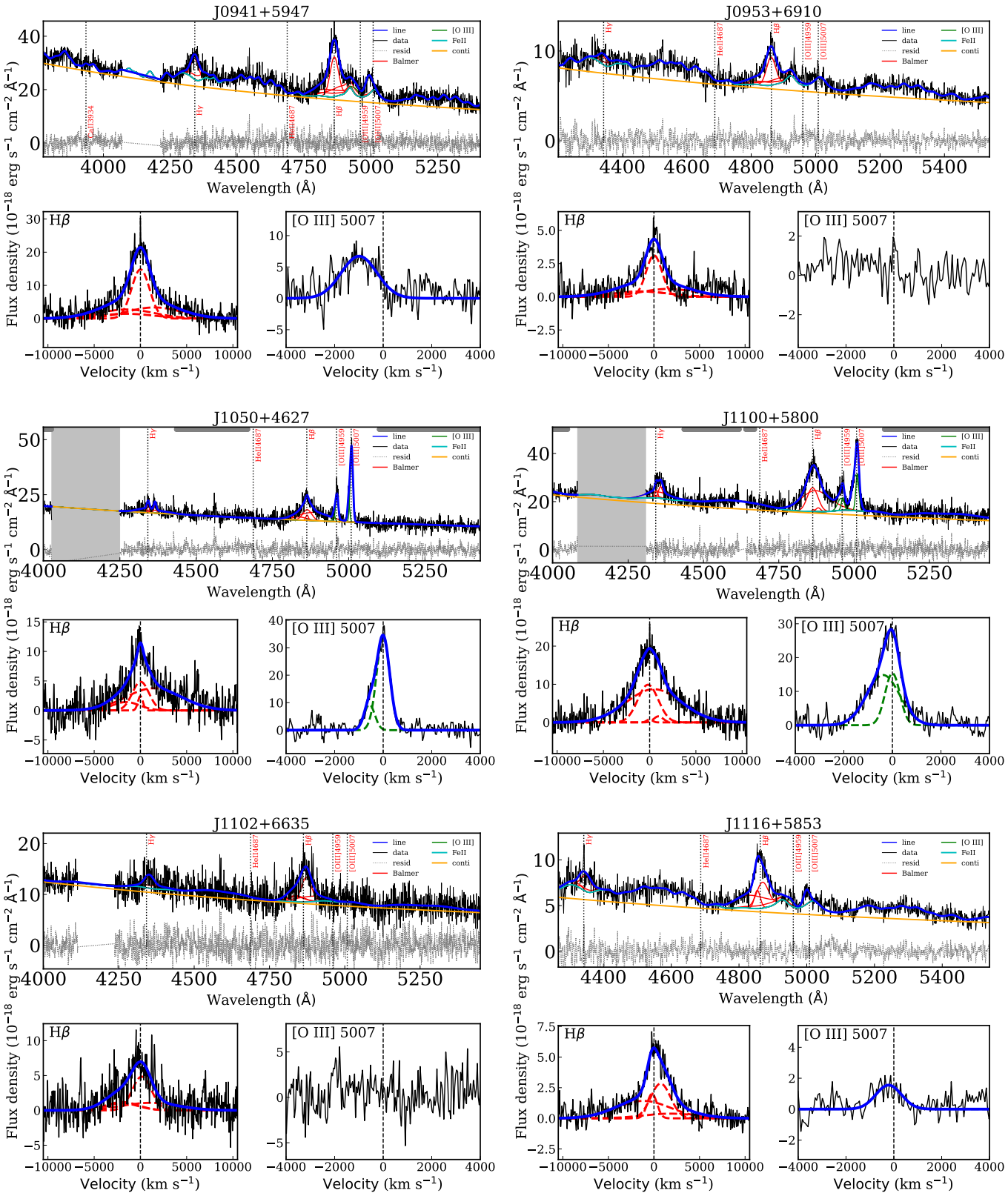

Figure 11. Continued

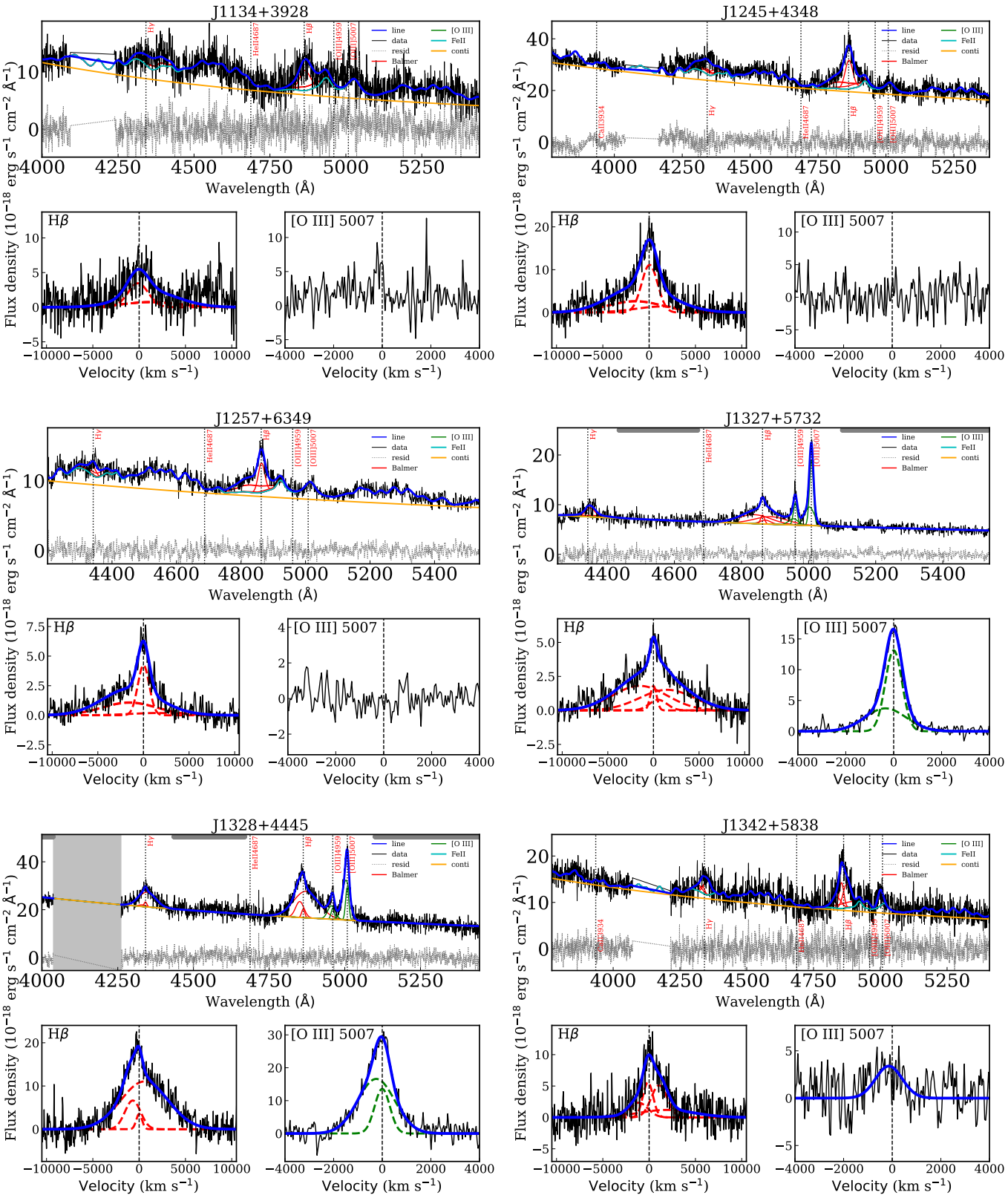

Figure 11. Continued

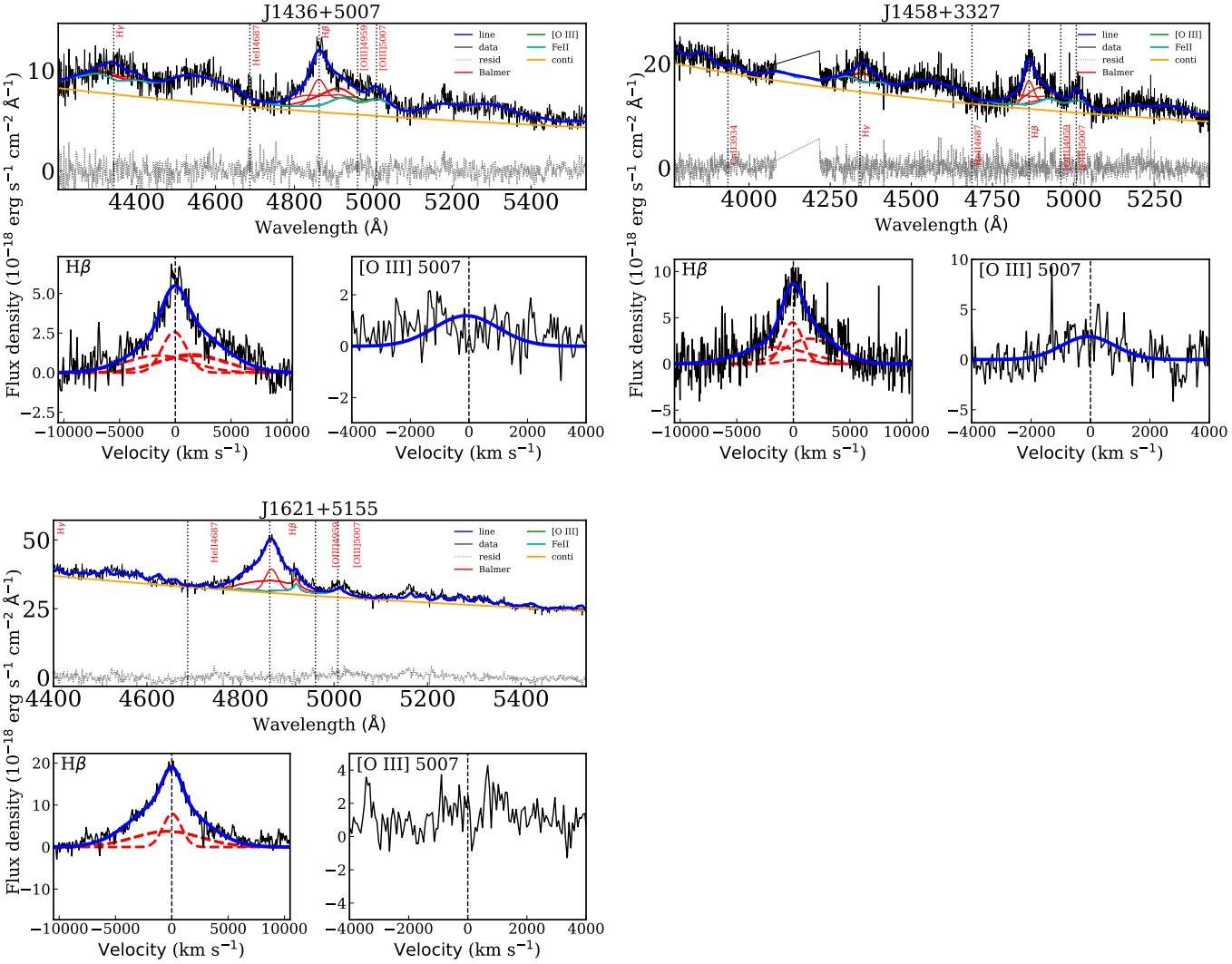

Figure 11. Continued

Dietrich, M., & Hamann, F. 2004, ApJ, 611, 761, doi: 10.1086/422382

Dietrich, M., Mathur, S., Grupe, D., & Komossa, S. 2009, ApJ, 696, 1998, doi: 10.1088/0004-637X/696/2/1998

Fan, X., Bañados, E., & Simcoe, R. A. 2023, Annual Review of Astronomy and Astrophysics, 61, 373, doi: 10.1146/annurev-astro-052920-102455

Fan, X., Wang, F., Yang, J., et al. 2019, ApJL, 870, L11, doi: 10.3847/2041-8213/aaeffe

Farina, E. P., Schindler, J.-T., Walter, F., et al. 2022, ApJ, 941, 106, doi: 10.3847/1538-4357/ac9626

Greene, J. E., & Ho, L. C. 2005, ApJ, 630, 122, doi: 10.1086/431897

Greene, J. E., Peng, C. Y., Kim, M., et al. 2010, ApJ, 721, 26, doi: 10.1088/0004-637X/721/1/26

Guo, H., Shen, Y., & Wang, S. 2018, PyQSOFit: Python code to fit the spectrum of quasars, Astrophysics Source Code Library. http://ascl.net/1809.008

Hewett, P. C., & Wild, V. 2010, MNRAS, 405, 2302, doi: 10.1111/j.1365-2966.2010.16648.x

Ho, L. C., Goldoni, P., Dong, X.-B., Greene, J. E., & Ponti, G. 2012, ApJ, 754, 11, doi: 10.1088/0004-637X/754/1/11

Hummer, D. G., & Storey, P. J. 1987, MNRAS, 224, 801, doi: 10.1093/mnras/224.3.801

Jakobsen, P., Ferruit, P., Alves de Oliveira, C., et al. 2022, A&A, 661, A80, doi: 10.1051/0004-6361/202142663

Kauffmann, G., et al. 2003, MNRAS, 346, 1055, doi: 10.1111/j.1365-2966.2003.07154.x

Keel, W. C., Chojnowski, S. D., Bennert, V. N., et al. 2012a, MNRAS, 420, 878, doi: 10.1111/j.1365-2966.2011.20101.x

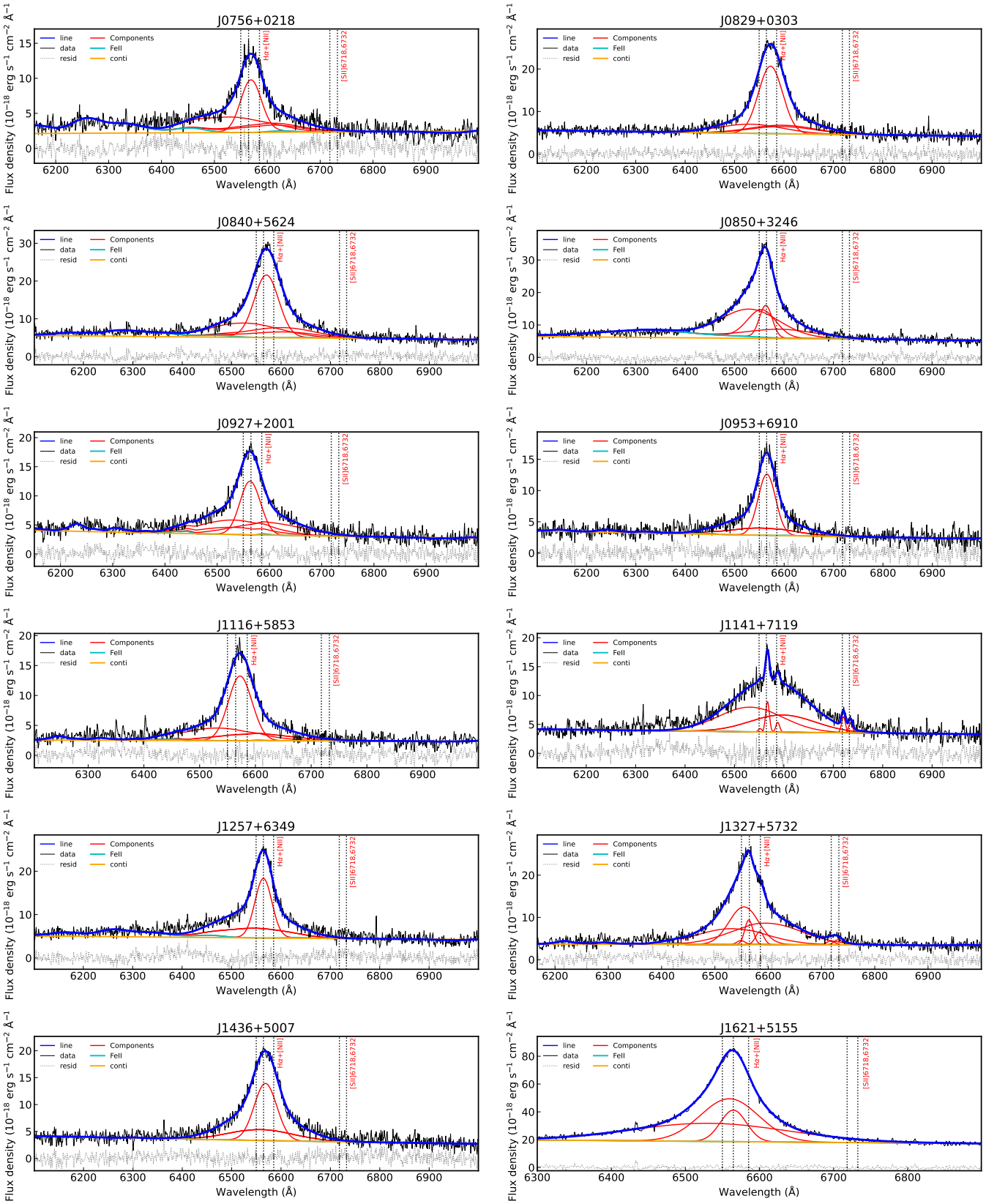

Figure 12. Spectra and best-fit models for the Hα region of the z $\sim$ 6 objects. The plotting styles are the same as in Fig. 11.

Keel, W. C., Lintott, C. J., Schawinski, K., et al. 2012b, AJ, 144, 66, doi: 10.1088/0004-6256/144/2/66

Keel, W. C., Bennert, V. N., Pancoast, A., et al. 2019, MNRAS, 483, 4847, doi: 10.1093/mnras/sty3332

Kewley, L. J., Dopita, M. A., Sutherland, R. S., Heisler, C. A., & Trevena, J. 2001, ApJ, 556, 121, doi: 10.1086/321545

Kewley, L. J., Dopita, M. A., Sutherland, R. S., Heisler, C. A., & Trevena, J. 2001, ApJ, 556, 121, doi: 10.1086/321545

Li, Q., Conselice, C. J., Duan, Q., et al. 2025, arXiv e-prints, arXiv:2508.09749, doi: 10.48550/arXiv.2508.09749

Lintott, C. J., Schawinski, K., Keel, W., et al. 2009, MNRAS, 399, 129, doi: 10.1111/j.1365-2966.2009.15299.x

Liu, G., Zakamska, N. L., Greene, J. E., Nesvadba, N. P. H., & Liu, X. 2013, MNRAS, 436, 2576, doi: 10.1093/mnras/stt1755

Liu, W., Veilleux, S., Canalizo, G., et al. 2020, ApJ, 905, 166, doi: 10.3847/1538-4357/abc269

Liu, W., Fan, X., Yang, J., et al. 2024, ApJ, 976, 33, doi: 10.3847/1538-4357/ad7de4

Liu, W., Fan, X., Li, H., et al. 2025, Frequent Extreme Galaxy-scale Outflows among Luminous Early Quasars. https://arxiv.org/abs/2509.08793

Liu, W., Veilleux, S., Sankar, S., et al. 2025, ApJ, 980, 31, doi: 10.3847/1538-4357/ada772

Loiacono, F., Decarli, R., Mignoli, M., et al. 2024, arXiv e-prints, arXiv:2402.13319, doi: 10.48550/arXiv.2402.13319

Lyu, J., Rieke, G. H., Stone, M., et al. 2025, ApJL, 981, L20, doi: 10.3847/2041-8213/adb613

Maiolino, R., Scholtz, J., Curtis-Lake, E., et al. 2024, A&A, 691, A145, doi: 10.1051/0004-6361/202347640

Marshall, M. A., Perna, M., Willott, C. J., et al. 2023, A&A, 678, A191, doi: 10.1051/0004-6361/202346113

Marshall, M. A., Yue, M., Eilers, A.-C., et al. 2024, arXiv e-prints, arXiv:2410.11035, doi: 10.48550/arXiv.2410.11035

Marshall, M. A., Windhorst, R. A., Ferrami, G., et al. 2025, arXiv e-prints, arXiv:2502.20550, doi: 10.48550/arXiv.2502.20550

Marziani, P., Sulentic, J. W., Zamanov, R., et al. 2003, ApJS, 145, 199, doi: 10.1086/346025

Marziani, P., Sulentic, J. W., Zwitter, T., Dultzin-Hacyan, D., & Calvani, M. 2001, ApJ, 558, 553, doi: 10.1086/322286

Matsuoka, Y., Onoue, M., Kashikawa, N., et al. 2019, ApJL, 872, L2, doi: 10.3847/2041-8213/ab0216

Matsuoka, Y., Izumi, T., Onoue, M., et al. 2024, ApJL, 965, L4, doi: 10.3847/2041-8213/ad35c7

Matthews, B. M., Dix, C., Shemmer, O., et al. 2023, ApJ, 950, 95, doi: 10.3847/1538-4357/acd04c

McLure, R. J., & Dunlop, J. S. 2004, MNRAS, 352, 1390, doi: 10.1111/j.1365-2966.2004.08034.x

McLure, R. J., & Jarvis, M. J. 2002, MNRAS, 337, 109, doi: 10.1046/j.1365-8711.2002.05871.x

Merluzzi, P., Busarello, G., Dopita, M. A., et al. 2018, ApJ, 852, 113, doi: 10.3847/1538-4357/aa9fff

Moiseev, A. V., Smirnova, A. A., & Movsessian, T. A. 2023, Universe, 9, 493, doi: 10.3390/universe9120493

Moran, E. C., Halpern, J. P., Bothun, G. D., & Becker, R. H. 1992, AJ, 104, 990, doi: 10.1086/116292

Nesvadba, N. P. H., Lehnert, M. D., De Breuck, C., Gilbert, A. M., & van Breugel, W. 2008, A&A, 491, 407, doi: 10.1051/0004-6361:200810346

Netzer, H., Shemmer, O., Maiolino, R., et al. 2004, ApJ, 614, 558, doi: 10.1086/423608

Netzer, H., & Trakhtenbrot, B. 2007, ApJ, 654, 754, doi: 10.1086/509650

Onoue, M., Kashikawa, N., Matsuoka, Y., et al. 2019, ApJ, 880, 77, doi: 10.3847/1538-4357/ab29e9

Osterbrock, D. E., & Ferland, G. J. 2006, Astrophysics of gaseous nebulae and active galactic nuclei (Sausalito, CA: University Science Books)

Osterbrock, D. E., & Shuder, J. M. 1982, ApJS, 49, 149, doi: 10.1086/190793

Pâris, I., Petitjean, P., Ross, N. P., et al. 2017, A&A, 597, A79, doi: 10.1051/0004-6361/201527999

Perna, M., Brusa, M., Cresci, G., et al. 2015, A&A, 574, A82, doi: 10.1051/0004-6361/201425035

Plotkin, R. M., Shemmer, O., Trakhtenbrot, B., et al. 2015, ApJ, 805, 123, doi: 10.1088/0004-637X/805/2/123

Protušová, K., Bosman, S. E. I., Wang, F., et al. 2024, arXiv e-prints, arXiv:2412.12256, doi: 10.48550/arXiv.2412.12256

Rauscher, B. J. 2024, PASP, 136, 015001, doi: 10.1088/1538-3873/ad1b36

Richards, G. T., Fan, X., Newberg, H. J., et al. 2002, AJ, 123, 2945, doi: 10.1086/340187

Richards, G. T., Lacy, M., Storrie-Lombardi, L. J., et al. 2006, ApJS, 166, 470, doi: 10.1086/506525

Richards, G. T., Kruczek, N. E., Gallagher, S. C., et al. 2011, AJ, 141, 167, doi: 10.1088/0004-6256/141/5/167

Runnoe, J. C., Brotherton, M. S., Shang, Z., Wills, B. J., & DiPompeo, M. A. 2013, MNRAS, 429, 135, doi: 10.1093/mnras/sts322

Schawinski, K., Evans, D. A., Virani, S., et al. 2010, ApJL, 724, L30, doi: 10.1088/2041-8205/724/1/L30

Schindler, J.-T., Farina, E. P., Bañados, E., et al. 2020, ApJ, 905, 51, doi: 10.3847/1538-4357/abc2d7

Schirmer, M., Diaz, R., Holhjem, K., Levenson, N. A., & Winge, C. 2013, ApJ, 763, 60, doi: 10.1088/0004-637X/763/1/60
Scholtz, J., Maiolino, R., D'Eugenio, F., et al. 2023, arXiv e-prints, arXiv:2311.18731, doi: 10.48550/arXiv.2311.18731
Shemmer, O., & Lieber, S. 2015, ApJ, 805, 124, doi: 10.1088/0004-637X/805/2/124
Shen, Y. 2013, Bulletin of the Astronomical Society of India, 41, 61, doi: 10.48550/arXiv.1302.2643
—. 2016, ApJ, 817, 55, doi: 10.3847/0004-637X/817/1/55
Shen, Y., Greene, J. E., Strauss, M. A., Richards, G. T., & Schneider, D. P. 2008, ApJ, 680, 169, doi: 10.1086/587475
Shen, Y., & Ho, L. C. 2014, Nature, 513, 210, doi: 10.1038/nature13712
Shen, Y., & Liu, X. 2012, ApJ, 753, 125, doi: 10.1088/0004-637X/753/2/125
Shen, Y., Richards, G. T., Strauss, M. A., et al. 2011, ApJS, 194, 45, doi: 10.1088/0067-0049/194/2/45
Shen, Y., Wu, J., Jiang, L., et al. 2019, ApJ, 873, 35, doi: 10.3847/1538-4357/ab03d9
Stern, J., & Laor, A. 2013, MNRAS, 431, 836, doi: 10.1093/mnras/stt211
Sulentic, J. W., Repetto, P., Stirpe, G. M., et al. 2006, A&A, 456, 929, doi: 10.1051/0004-6361:20054153
Sulentic, J. W., Stirpe, G. M., Marziani, P., et al. 2004, A&A, 423, 121, doi: 10.1051/0004-6361:20035912
Trakhtenbrot, B., Netzer, H., Lira, P., & Shemmer, O. 2011, ApJ, 730, 7, doi: 10.1088/0004-637X/730/1/7
Vanden Berk, D. E., Richards, G. T., Bauer, A., et al. 2001, AJ, 122, 549, doi: 10.1086/321167
Vayner, A., Zakamska, N. L., Ishikawa, Y., et al. 2023, ApJ, 955, 92, doi: 10.3847/1538-4357/ace784
Veilleux, S., Liu, W., Vayner, A., et al. 2023, ApJ, 953, 56, doi: 10.3847/1538-4357/ace10f
Vestergaard, M. 2002, ApJ, 571, 733, doi: 10.1086/340045
Vestergaard, M., & Peterson, B. M. 2006a, ApJ, 641, 689, doi: 10.1086/500572
—. 2006b, ApJ, 641, 689, doi: 10.1086/500572
Vestergaard, M., & Wilkes, B. J. 2001, ApJS, 134, 1, doi: 10.1086/320357
Volonteri, M. 2012, Science, 337, 544, doi: 10.1126/science.1220843
Wang, F., Wu, X.-B., Fan, X., et al. 2016, ApJ, 819, 24, doi: 10.3847/0004-637X/819/1/24
Wang, F., Yang, J., Fan, X., et al. 2021, The Astrophysical Journal, 907, L1, doi: 10.3847/2041-8213/abd8c6
Wang, F., Yang, J., Hennawi, J. F., et al. 2023, The Astrophysical Journal Letters, 951, L4, doi: 10.3847/2041-8213/accd6f
Wu, X.-B., Wang, F., Fan, X., et al. 2015, Nature, 518, 512, doi: 10.1038/nature14241
Wu, Y., Wang, F., Cai, Z., et al. 2023, The Astrophysical Journal Letters, 956, L40, doi: 10.3847/2041-8213/acfee3
Yang, J., Wang, F., Fan, X., et al. 2021, ApJ, 923, 262, doi: 10.3847/1538-4357/ac2b32
—. 2023, ApJL, 951, L5, doi: 10.3847/2041-8213/acc9c8
Yue, M., Fan, X., Yang, J., & Wang, F. 2023, AJ, 165, 191, doi: 10.3847/1538-3881/acc2be
Zhang, K., Wang, T.-G., Gaskell, C. M., & Dong, X.-B. 2013, ApJ, 762, 51, doi: 10.1088/0004-637X/762/1/51
Zhu, Y., Egami, E., Fan, X., et al. 2025, arXiv e-prints, arXiv:2509.00153. https://arxiv.org/abs/2509.00153
Zuo, W., Wu, X.-B., Fan, X., et al. 2015, ApJ, 799, 189, doi: 10.1088/0004-637X/799/2/189